

Mem3DG: Modeling Membrane Mechanochemical Dynamics in 3D using Discrete Differential Geometry

C. Zhu¹, C. T. Lee^{1*}, and, P. Rangamani^{1*}

¹Department of Mechanical and Aerospace Engineering, University of California San Diego, La Jolla CA 92093;

*To whom correspondence must be addressed: ctlee@ucsd.edu, prangamani@ucsd.edu

Abstract

Biomembranes adopt varying morphological configurations that are vital to cellular functions. Many studies use computational modeling to understand how various mechanochemical factors contribute to membrane shape transformations. Compared to traditional approximation-based methods (e.g., finite element method), the class of discrete mesh models offers greater flexibility to simulate complex physics and shapes in three dimensions; its formulation produces an efficient algorithm while maintaining expressive coordinate-free geometric descriptions. However, ambiguities in geometric definitions in the discrete context have led to a lack of consensus on which discrete mesh based model is theoretically and numerically optimal; a bijective relationship between the terms contributing to both the energy and forces from the discrete and smooth geometric theories remains to be established. We address this and present an extensible framework, Mem3DG, for modeling 3D mechanochemical dynamics of membranes based on [Discrete Differential Geometry \(DDG\)](#) on triangulated meshes. The formalism of [DDG](#) resolves the inconsistency and provides a unifying perspective on how to relate the smooth and discrete energy and forces. Mem3DG is designed to facilitate models in tandem with and mimicking experimental studies. It also supports the use of realistic membrane ultrastructure from 3D imaging as an input. To demonstrate, Mem3DG is used to model a sequence of examples with increasing mechanochemical complexity: recovering classical shape transformations such as 1) biconcave disk, dumbbell, and unduloid and 2) spherical bud on spherical, flat-patch membrane; investigating how the coupling of membrane mechanics with protein mobility jointly affects phase and shape transformation. While the first two examples serve as validation, the later examples provide a blueprint for extending Mem3DG to model a system of interest. As high-resolution 3D imaging of membrane ultrastructure becomes more readily available, we envision Mem3DG to be applied as an end-to-end tool to simulate realistic cell geometry under user-specified mechanochemical conditions. We hope that Mem3DG will be a useful tool to help advance the mission of computational membrane mechanobiology.

1 Introduction

Computational modeling of lipid bilayer mechanics has long been accepted as a way to probe the biophysical aspects of membrane curvature generation. The ability of lipid bilayers and cellular membranes to bend in response to various applied forces has been studied extensively from the mathematical modeling perspective. However, the nonlinear system of equations that result from such modeling often leads to a computational bottleneck to generate predictions from simulations that can be tested against experimentally observed shapes. In this study, we develop a mesh-based model using discrete differential geometry to reduce this bottleneck. To justify why our method is necessary and is a computational advance, we first describe the importance of membrane curvature generation in biology, the current state-of-the-art in membrane mechanics modeling, and finally explicitly state the goals of our approach.

1.1 Membrane curvature generation in biology

As one of the most essential and conserved structures of cells, cellular membranes perform many functions. First, they form compartments to separate chemical environments. Beyond the passive role of partitioning space, lipids in the membranes interact with proteins and other cellular components influencing cell signaling

(e.g., by localizing molecules and acting as an entropic barrier) (1, 2). Membrane morphology and topology changes are critical for trafficking cargo in and out of cells and are very carefully regulated (3–8). Central to these roles is the ability of the membrane to curve and adopt varying morphological configurations from spheres to highly-curved and variegated structures.

Advances in experimental studies of membrane–protein interactions (9–20), ultrastructural imaging (21–30), and image analysis (9–11, 31–37) have revealed much about the molecular interactions that regulate membrane curvature. To investigate the mechanics behind these interactions, many theoretical and computational models in terms of membrane energetics and thermodynamics have been developed (7, 38–52). These models, owing to the ease of *in silico* experimentation, have become an important tool for generating and testing hypotheses (53, 54). These mechanics models and associated simulations have been used to provide intuition on the mechanical requirements for forming and maintaining complex cellular membrane shapes (55–63).

While the utility of this approach has been established and many models have been developed (38), many models are limited by critical assumptions or other technical challenges. For example, the ability to use geometries from membrane ultrastructural imaging experiments as a starting condition would improve model realism (64). With respect to computational complexity, the solver should be able to model deformations and topological changes in three dimensions and be compatible with both energy minimization and time-integration for comparing with static and time-series experiments respectively. This is in contrast to the current assumptions of the existence of an axis of symmetry that is quite commonly made for purposes of ease of simulation (65). An additional feature for these solvers should be that their implementation is modular such that the addition of new physics or increasing model complexity should be straightforward. This includes the potential for coupling the membrane model with agent-based and other simulations to propagate other cellular components such as the cytoskeleton (66). Thus, new computational tools which are general, easy to use, and without restrictive assumptions are needed to bring modeling closer to experimental observations of membrane shapes in cells.

69 1.2 State-of-the-art membrane modeling

70 To emphasize the motivations behind our choice of extending and developing a new mesh-based membrane
71 model, we provide a brief summary of the legacy literature in modeling membrane mechanics. The most com-
72 mon theoretical model of membrane bending is the Helfrich-Canham-Evans Hamiltonian,¹ which describes
73 the lipid bilayer as a two-dimensional fluid-like structure that exhibits solid-like elasticity in the out-of-plane
74 direction (39, 40, 68–70). It is a continuum model which describes the bending energy of the membrane as
75 a function of its mean and Gaussian curvatures. The assumptions for the continuum are satisfied as long as
76 the deformations are much larger in length scale compared to the individual lipid components.

77 Given the necessary material properties and boundary conditions, by minimizing the Helfrich energy, we
78 can obtain the equilibrium shape of the membrane (39, 70–72). While straightforward in concept, energy
79 minimization requires the determination of the forces on the membrane which is a challenging task (65). The
80 forces on the membrane are given by the variation of the energy with respect to the embedded coordinate (i.e.,
81 shape) of the membrane². Taking the shape derivatives of the Helfrich energy produces the “shape equation”,
82 so termed because solutions of this partial differential equation, with the prescribed boundary conditions,
83 produce configurations at equilibrium (i.e., force-balance).

84 Solving the shape equation is non-trivial since it is a partial differential equation with fourth-order nonlinear
85 terms. As a result, analytical solutions of the shape equation are known only for a few cases constrained to
86 specific geometries and boundary conditions (42). For most systems, we must resort to the use of numerical
87 methods. The simplest numerical schemes can be formulated by making restrictive assumptions such as
88 considering only small deformations from a plane (e.g., Monge parametrization) or assuming that there exists
89 an axis of symmetry such that the resulting boundary value system can be integrated (38). While these

¹The Helfrich energy is related to the Willmore energy in the mathematics literature (67)

²We call this variation the shape derivative which is distinct from the chemical derivative that will be introduced later in the context of mechanochemical coupling

90 methods are suitable for idealized shapes, these assumptions are not consistent with the membrane shapes
 91 found in biology are and thus not general enough for advancing the field.

Table 1: Comparison of common mathematical frameworks for modeling membrane mechanics with specifications to advance the mission of computational membrane mechanobiology. A general framework will permit the easy transfer of inputs and results between model and experiments. Models which can be coupled with other modeling schemes representing other cellular components can help address the complexity of cell biology. Discrete mesh models have many desirable traits, with respect to these specifications, at the cost of forgoing rigorous error analysis.

	Phase field/level set	FEM	Discrete Mesh/Mem3DG
General 3D	✓	✓	✓
Statics + dynamics	✓	✓	✓
Membrane heterogeneity	✓	✓	✓
Compatibility with agent/particle			✓
Compatible with stochastic dynamics (e.g., DPD or MC)			✓
Explicit surface parametrization		✓	✓
Implementation preserves geometric intuition			✓
Ability to support topological changes	✓		requires mesh surgery
Error analysis	✓	✓	

92 Solvers of membrane shape in 3D have also been developed and can be categorized into three groups:
 93 1) phase field or level set methods (73–75), 2) Finite Element Method (FEM) (76–83), and 3) discrete surface
 94 mesh models (60, 84–94). These methods and others, reviewed in detail by Guckenberger *et al.* (95), differ
 95 in the strategy used to discretize the membrane domain and compute the relevant derivatives. We compare
 96 the aforementioned general, 3D models to our established model criteria in Table 1 and elaborate below.

97 Phase field and level set methods solve the shape equation by propagating a density field on an ambient
 98 volumetric mesh. The membrane shape is implicit in these models and can be found by drawing an isosur-
 99 face or level set of the model. While this is ideal for modeling membrane topological changes, the implicit
 100 representation of the membrane adds complexity for interfacing with data generated using modern methods
 101 of visualizing membrane ultrastructure. The meshes output from ultrastructural studies must be converted
 102 into a density or phase field prior to input to the model. While this conversion is possible, representing the
 103 dynamic and variegated shapes of cellular membranes would require a dense volume mesh, which reduces
 104 computational tractability. The implicit surface representation also complicates the addition of new in-plane
 105 physics for end-users.

106 FEM and discrete mesh models use an explicit surface parametrization (i.e., a mesh). Thus the meshes
 107 output from ultrastructural imaging datasets can be used in these frameworks with minor modifications (32,
 108 96). Comparing FEM methods with our specifications we identify a few key challenges. First, the numerical
 109 evaluation of smooth geometric measurements on arbitrary manifolds in an FEM framework requires non-
 110 intuitive tensor algebra to translate the shape equation in coordinate where it is ready to be solved. After
 111 this formulation, solving the shape equation can require the use of high order function basis such as the
 112 C^1 conforming FEM based on subdivision scheme (76, 77) or isogeometric analysis (IGA) (79–81, 83), which
 113 adds code complexity and run-time cost. Extending an FEM framework to incorporate new physics, topological
 114 changes, or interfaces with other models requires advanced mathematical and coding skills. This can restrict
 115 the usage to the computational math community and prevent broad usage by the biophysics community.

116 Finally, evaluating discrete mesh-based methods, which define the system energy and/or forces using
117 geometric primitives from a mesh, we find that they satisfy many of the requirements in Table 1. Due to the
118 ease of use and implementation, discrete mesh models have gained in popularity and many different schemes
119 can be found in the literature (60, 84–94, 97, 98). These schemes differ in their approach to defining and
120 computing geometric measures necessary for defining the energy and forces on a discrete object. Discrete
121 geometries have discontinuities and limited information that leads to degenerate definitions for geometric
122 values. For example, there is no canonical definition for the normal of a vertex of a mesh as opposed to
123 the normal of a smooth geometry (87, 99, 100). One challenge for selecting the suitable formulation to use
124 is the lack of approximation error metric for which the discrete definition best matches the smooth theory.
125 Another confounding factor is the step at which the problem is discretized. Some implementations discretize
126 the energy of the system by constructing standalone discrete energy, which captures the behavior of the
127 Helfrich energy (65). From this discrete energy, they take the shape derivatives to obtain an expression for
128 the discrete force. Without careful consideration, the discrete forces derived in this manner are unstructured
129 and there is little resemblance to expressions of force from smooth theory. A second option is to discretize
130 the smooth force expression directly (65, 95). While this preserves the geometric connection for the forces,
131 there is no longer well-defined discrete energy. Several discrete mesh methods were benchmarked by Bian
132 *et al.* (87) and Guckenberger *et al.* (95) who found differences in the accuracy, robustness, and ease of
133 implementation (87, 95).

134 1.3 Goals of the current work

135 In this work, we outline a discrete mesh framework for modeling membrane mechanics with the following
136 goals in mind: (a) we do not make *a priori* assumptions about axes of symmetry or restrict the coordinates in
137 any way; (b) we resolve the ambiguity in the definition of geometric measures on the mesh and permit direct
138 comparison for both the energy and force expressions in smooth and discrete contexts; and (c) this framework
139 allows for use of meshes generated from ultrastructural imaging. We begin by defining a discrete energy that
140 is analogous to the Helfrich energy. Then using concepts from DDG, we derive discrete shape derivatives and
141 group terms to produce a discrete shape equation. We will show that our discrete shape equation has a clear
142 correspondence between the terms of the smooth shape equations (57, 67, 70, 71). Beyond establishing this
143 important connection, we will show that the elegant analytical expressions for discrete variational terms from
144 the DDG also yield improved geometric intuition and numerical accuracy (99, 100).

145 Benchmarking of our expressions was performed with our accompanying software implementation called
146 Membrane Dynamics in 3D using Discrete Differential Geometry (Mem3DG). Mem3DG is written in C++, released
147 under the Mozilla Public License version 2, and comes with accompanying documentation and tutorials which
148 can be accessed on GitHub (<https://github.com/RangamaniLabUCSD/Mem3DG>). Beyond the computation
149 of discrete energies and forces on a mesh of interest, we also include functionality for performing energy
150 minimization and time integration. Using Mem3DG, we validate the exactness of the analytical expressions
151 of force terms by numerically examining the convergence of the force terms as a function of system energy
152 perturbation. To illustrate compliance with our tool specifications, we apply Mem3DG to a sequence of examples
153 with increasing complexity. Finally, we outline the steps to incorporate additional physics such as membrane-
154 protein interactions and surface diffusion into Mem3DG.

155 2 Methods

156 The lipid bilayer is modeled as a thin elastic, incompressible shell using the Helfrich-Canham-Evans Hamil-
157 tonian or spontaneous curvature model (39, 69, 101). The bending energy, E_b , of a smooth surface or 2-
158 manifold, \mathcal{M} , can be expressed in terms of the mean H , Gaussian K , and spontaneous curvature \bar{H} with
159 material parameters κ the bending and κ_G the saddle-splay moduli. Additional energy terms E_s and E_p ac-
160 count for the tension–area ($\lambda-A$) and pressure–volume ($\Delta P-V$) relationships; The total energy of the bilayer

161 is therefore

$$E = \underbrace{\int_{\mathcal{M}} [\kappa(H - \bar{H})^2 + \kappa_G K] dA}_{E_b} + \underbrace{\int_{\bar{A}} \lambda d\tilde{A}}_{E_s} - \underbrace{\int_{\bar{V}} \Delta P d\tilde{V}}_{E_p}. \quad (1)$$

162 The preferred surface area and volume, \bar{A} and \bar{V} , combined with the spontaneous curvature, \bar{H} , characterize
 163 the zero-energy state for the system energy. In a nutshell, given the material properties, the system energy
 164 is fully determined by its geometric measurements such as volume, area, and curvatures.

165 Machinery to express these measurements have been a topic of extensive study in classical differential
 166 geometry (102, 103). However, finding the minima of the governing energy, solving the stationary solution to
 167 the geometric Partial Differential Equation (PDE), can be mathematically and numerically difficult. While dif-
 168 ferential geometry provides succinct expressions to describe the measurements in a coordinate-free fashion,
 169 computational methods often require the introduction of a coordinate basis and subsequent manipulation of
 170 expressions using tensor algebra, which can obscure the underlying geometric intuition.

171 As an alternative, forgoing the need for a smooth geometry, one can treat a discrete geometry (such as
 172 a geometric mesh) as the input. This perspective where the discrete geometry is the actual geometry is that
 173 of DDG. By eliminating the burdens of treating the input mesh as an approximation of a smooth object, DDG
 174 capitalizes upon the piecewise nature of meshes to produce efficient and parallelizable finite difference-like
 175 formulae which are amenable to algorithmic implementation while maintaining clear geometric meaning. In the
 176 following sections, we use concepts from DDG to formulate a discrete analog to the smooth membrane shape
 177 problem. Following the derivation of the discrete theory, we describe the development of an accompanying
 178 software implementation called Mem3DG.

179 2.1 Notation and preliminaries

180 We assume the following notation conventions and provide a table of important symbols (Table 2). To aid the
 181 reader on how the elements of the mesh are used in the derivation, several fundamental geometric primitives
 182 (i.e., values on a mesh which are easily measurable; listed in Table 2A) are illustrated in Fig. 1A-C.

183 We note that in discrete contexts the notation, $\int a$, should be considered the discrete (integrated) counter-
 184 part of a pointwise measurement a in a smooth setting. The rationale and significance behind the usage of an
 185 integrated measure in discrete contexts are elaborated in Appendix B and the DDG literature (99, 100). Using
 186 this notation, discrete surface integrals are expressed as sums of integrated values over the discrete mesh
 187 components listed in Table 2B (e.g., $\sum_{v_i} \int a_i$ is the discrete analog to $\int_{\mathcal{M}} a$). It is possible to interchange
 188 between integrated, $\int a_i$, and pointwise, a_i , measures by using the dual area (A_i),

$$a_i = \int a_i / A_i. \quad (2)$$

189 For simplicity, we will not use separate notations for operators applying in smooth and discrete settings. The
 190 context can be inferred from the objects to which the operators are applied. Where it serves to improve our
 191 geometric or other intuition, smooth objects will be presented alongside discrete objects for comparison.

192 2.2 Obtaining a discrete energy defined by mesh primitives

193 Following the perspective of DDG, we restrict our input to the family of triangulated manifold meshes, \mathcal{M} (i.e.,
 194 discrete 2-manifolds embedded in \mathbb{R}^3)³.

195 Paralleling the smooth Helfrich Hamiltonian (Eq. (1)), a functional of geometric measurements of a surface,
 196 the discrete Helfrich Hamiltonian is composed of discrete analog of those measurements,

$$E(\vec{r}) = \underbrace{\sum_{v_i} \left[\kappa_i \int (H_i - \bar{H}_i)^2 + \kappa_G \int K_i \right]}_{E_b} + \underbrace{\int_{\bar{A}} \lambda(\tilde{A}; \vec{r}) d\tilde{A}}_{E_s} - \underbrace{\int_{\bar{V}} \Delta P(\tilde{V}; \vec{r}) d\tilde{V}}_{E_p}. \quad (3)$$

³We will use \mathcal{M} for both the smooth and discrete surfaces.

Table 2: Glossary of commonly used symbols and conventions

A. Geometric primitives:

\mathcal{M}	smooth or discrete 2-manifold
$\vec{r} \in \mathbb{R}^3$	embedded coordinate of \mathcal{M}
l	edge length
\angle	corner angle
φ	dihedral angle
A	area of mesh cell, e.g., face A_{ijk} , edge A_{ij} and vertex A_i
\vec{n}	surface normal

B. Surface Integral:

$\int a$	integrated quantity over mesh cell e.g., $A_i a_i$ or $A_{ijk} a_{ijk}$
\sum_{v_i}	sum over all vertices v_i of the mesh
$\sum_{e_{ij}}$	sum over all edges e_{ij} of the mesh
$\sum_{f_{ijk}}$	sum over all faces f_{ijk} of the mesh
$\sum_{v_j \in N(a)}$	sum over the vertex v_j in the neighborhood of a
$\sum_{e_{ij} \in N(a)}$	sum over the edges e_{ij} in the neighborhood of a
$\sum_{f_{ijk} \in N(a)}$	sum over the face f_{ijk} in the neighborhood of a

C. Tensors:

$x \in \mathbb{R}$	scalar quantity
$x_{\text{index}}^{\text{type}}$	sub- and super-script convention e.g., $\int f_i^b$ is the bending force for vertex i
$\vec{x} \in \mathbb{R}^3$	vector quantity
$\mathbf{x} = \{x_i\}$	$(n \times 1)$ indexed scalar quantity
$\vec{\mathbf{x}} = \{\mathbf{x}_i\}$	$(n \times 3)$ indexed vector quantity
$\tilde{\mathbf{X}}$	matrix or tensor quantity

D. Derivatives:

$\nabla_{\vec{r}}$	shape derivative
∇_{ϕ}	chemical derivative
$\nabla_{\vec{\theta}}$	surface gradient
\dot{a}	time derivative
Δ_s	Laplace-Beltrami operator

E. Physical Variables:

E	energy
f	force density
μ	chemical potential
H	mean curvature
K	Gaussian curvature
A	surface area
V	enclosed volume
$\bar{\cdot}$	preferred state e.g., \bar{H} is the spontaneous curvature
$\phi \in [0, 1]$	protein density parameter
λ	membrane tension
ΔP	osmotic pressure across the membrane
κ	bending rigidity
κ_G	Gaussian modulus
K_A	stretching modulus
K_V	osmotic strength constant
\bar{c}	molar ambient concentration
n	molar quantity of enclosed solute
η	Dirichlet energy constant
ε	adsorption energy constant
ξ	membrane drag constant
B	protein mobility constant

197 In comparison with Eq. (1), H_i and K_i are pointwise mean and Gaussian curvature measurements on vertices,
 198 $\int (H_i - \bar{H}_i)^2$ is the integrated Willmore measure, and the smooth surface integral is replaced by its discrete
 199 analog (i.e. finite summation), \sum_{v_i} (Table 2B).

200 The geometric properties of a given membrane configuration can be connected to the system's energy
 201 through constitutive relations. In this work, we assume that the surface tension follows a linear stress-strain
 202 model(104),

$$\lambda(A; \vec{r}) = K_A \frac{A(\vec{r}) - \bar{A}}{\bar{A}}, \quad (4)$$

203 where \bar{A} is the preferred surface area of the membrane, and K_A is the stretching modulus of the membrane.
 204 The osmotic pressure can be defined based on the van't Hoff formula as

$$\Delta P(V; \vec{r}) = P_{\text{in}} - P_{\text{out}} = iRT \left(\frac{n}{\bar{V}} - \bar{c} \right), \quad (5)$$

205 where i , R , T , \bar{c} and n are the van't Hoff index, ideal gas constant, temperature, ambient molar concentration,
 206 and molar amount of the enclosed solute. Substituting these constitutive relations (Eqs. (4) and (5)) into the
 207 energy (Eq. (3)), we get explicit expressions for E_s and E_p ,

$$E(\vec{r}) = E_b(\vec{r}) + \underbrace{\frac{1}{2} K_A \frac{[A(\vec{r}) - \bar{A}]^2}{\bar{A}}}_{E_s} + \underbrace{iRTn [r_c - \ln r_c - 1]}_{E_p}, \quad (6)$$

208 where $r_c = \bar{c}/(n/V)$ is the ratio of the concentrations of the ambient and enclosed solutions. Note that the
 209 preferred volume, \bar{V} , which is needed to evaluate the integral in Eq. (3), is related to the parameters in
 210 Eq. (5) by $\bar{V} = n/\bar{c}$. If the system is around the isosmotic condition (e.g., $V \rightarrow \bar{V}$), the leading order of the
 211 energy is given as,

$$E_p \approx \frac{1}{2} K_V \frac{(V - \bar{V})^2}{\bar{V}^2}, \quad (7)$$

212 where $K_V \equiv iRTn$ groups the phenomenological parameters.

213 To compute the energy of a system, we must obtain values for several geometric measurements which
 214 appear in the discrete energy function (i.e., H , K , A , V , etc.). For measures such as the volume and area,
 215 there are clear approaches for their evaluation on a triangulated mesh: summing the areas of the triangular
 216 faces and summing over the signed volume of tetrahedra (Fig. 1E – osmotic pressure and surface tension).
 217 For other measures such as the discrete mean and Gaussian curvatures, additional care must be taken.
 218 While in smooth contexts these curvatures have unique definitions, in discrete contexts there are multiple
 219 approaches for their calculation. For example, the mean curvature can be computed via the application of the
 220 cotangent Laplacian, the kernel of the heat equation, or fitting polynomials to a local patch (65). As mentioned
 221 earlier, there are challenges with these approaches which can limit their numerical accuracy and obscure the
 222 connection to smooth theory. Here using discrete exterior calculus and identification of geometric invariants,
 223 we produce theoretically and numerically consistent discrete expressions.

224 Similar to the polygonal curve introduced in Appendix B, a triangulated mesh has zero curvature on facets
 225 and ill-defined curvature on edges and vertices. Using the Steiner view, the sharp corners formed by vertices
 226 and edges are “smoothened” with portions of spherical and cylindrical shells, which have well-defined mean
 227 curvature (Fig. 1D). Taking the limit as the radii of the cylinders and spheres decrease, the leading order
 228 contribution of total mean curvature is given by the Steiner formula on an edge,

$$\int H_{ij} = \frac{l_{ij} \varphi_{ij}}{2}, \quad (8)$$

229 referred to as the edge mean curvature, where l_{ij} is the length of edge e_{ij} , and φ_{ij} is the dihedral angle on e_{ij}
 230 (i.e., the angle formed by the face normals of the neighboring triangles incident to e_{ij}) (illustrated in Fig. 1B).
 231 While not necessary, a triangulated mesh is often realized in \mathbb{R}^3 via vertex positions; thus it is conventional to

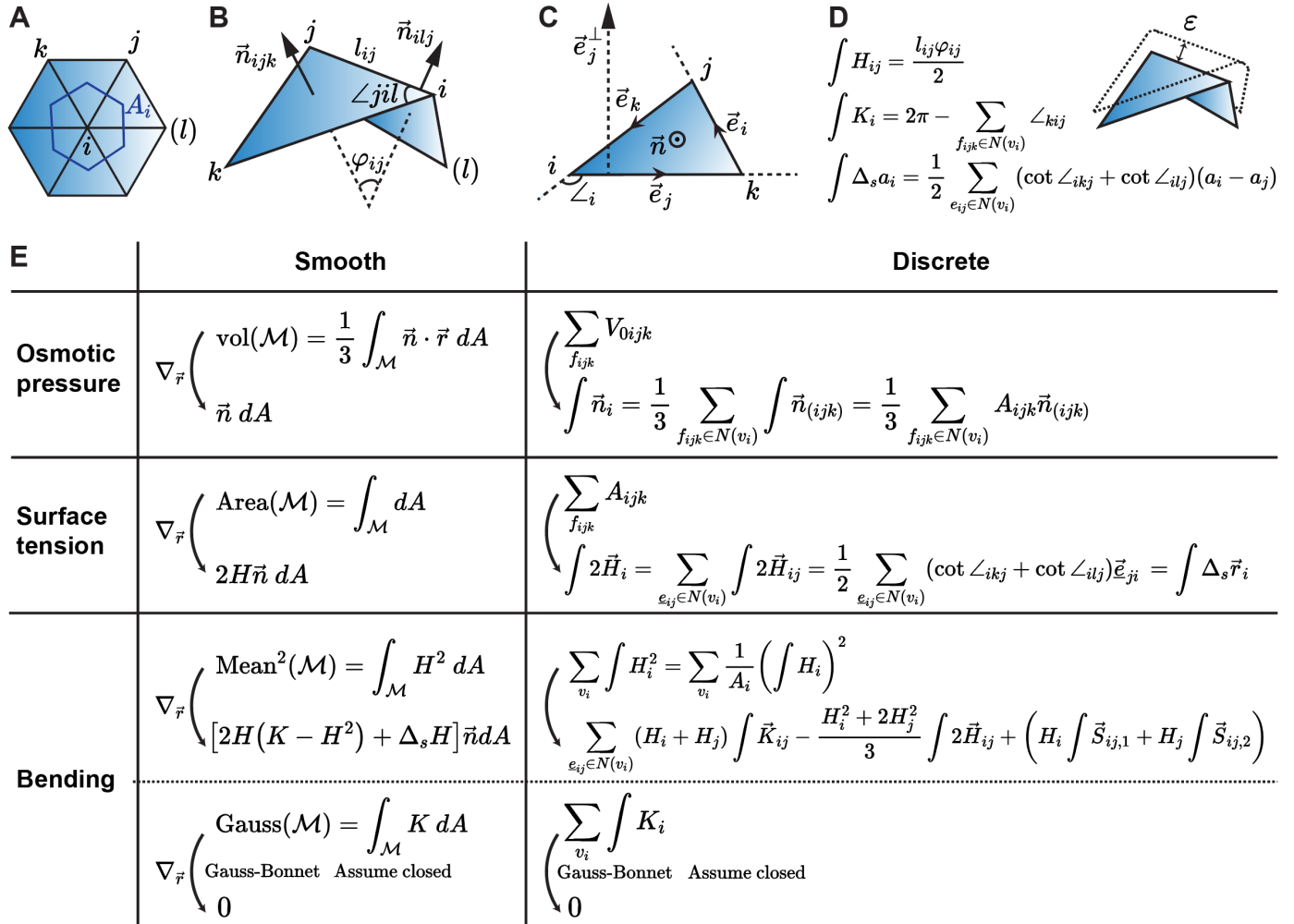


Figure 1: Overview of the DDG framework. A, B, C) Illustrations of geometric primitives in the neighborhood of A) Fan around a vertex, B) Diamond around an edge, and C) Triangle on a face. D) Discrete definition of scalar edge mean curvature, $\int H_{ij}$, scalar vertex Gaussian curvature, $\int K_i$, and Laplace-Beltrami operator, $\int \Delta_s(\cdot)$. E) Comparative derivation of Helfrich shape equation in both smooth and discrete formulation.

232 prescribe data on vertices instead of edges. Summation of edgewise quantities over the “fan” neighborhood
 233 (Fig. 1A) provides the recipe of converting an edgewise to a vertexwise measure,

$$(\cdot)_i = \frac{1}{2} \sum_{e_{ij} \in N(v_i)} (\cdot)_{ij}, \quad (9)$$

234 where the prefactor, $1/2$, accounts for fact that each edge is shared by two vertices.

235 While we have an integrated mean curvature, the discrete Helfrich Hamiltonian contains a pointwise mean
 236 curvature squared term. To define a pointwise mean curvature, the size of the domain *occupied* by the
 237 integrated mean curvature needs to be specified (c.f., Appendix B for rationale). The area, A_i , referred to
 238 as the dual area of the vertex v_i , can be defined as one-third of the areal sum of the incident triangles (“fan”
 239 illustrated in Fig. 1A). Applying Eqs. (2) and (9) to Eq. (8), the pointwise mean curvature is thus,

$$H_i = \frac{\int H_i}{A_i} = \sum_{e_{ij} \in N(v_i)} \frac{l_{ij} \varphi_{ij}}{4A_i}. \quad (10)$$

240 Substituting Eq. (10) into the integrated Willmore measure term of Eq. (3), the integrated Willmore measure
 241 can be expressed as a function of the integrated mean and spontaneous curvature,

$$\int (H_i - \bar{H}_i)^2 = \frac{1}{A_i} \left(\int H_i - \int \bar{H}_i \right)^2. \quad (11)$$

242 Discrete Gaussian curvature is given by the angle defect formula,

$$\int K_i = 2\pi - \sum_{f_{ijk} \in N(v_i)} \angle_{kij}, \quad (12)$$

243 which is a well-known measure that preserves many properties parallel to the smooth theory (e.g., Gauss-
 244 Bonnet, turning number, among other invariants). One way to derive the angle defect formula is to compute
 245 the area of a spherical n -gon contained by a local Gauss map of the neighboring n faces around a vertex (99,
 246 100). The discrete Gauss-Bonnet theorem states that

$$\sum_{v_i} \int K_i = 2\pi \chi(\mathcal{M}) - \sum_{e_{ij} \in \partial \mathcal{M}} \int \kappa_{ij}^g, \quad (13)$$

247 where $\chi(\mathcal{M}) = |V| - |E| + |F|$ is the Euler characteristic of \mathcal{M} , a topological invariant where $|V|$, $|E|$ and $|F|$
 248 represent the number of vertices, edges and faces of the mesh respectively. The discrete geodesic curvature,
 249 $\int \kappa^g$, is the discrete curvature of the boundary curve, $\partial \mathcal{M}$, as introduced and defined in Appendix B. When
 250 the surface \mathcal{M} is closed and does not undergo topological changes, the boundary term drops out and the
 251 total Gaussian curvature is a constant multiple of 2π . When surface \mathcal{M} is open, the geodesic curvature is
 252 integrated over one or more closed boundary loops, $\partial \mathcal{M}$. This integral, referred to as the turning number of
 253 a closed polygon, is invariant under regular homotopy (i.e., continuous deformation during which the curve
 254 stays regular) (99), which is admitted by the deformation of all membrane boundaries considered in this study.
 255 In summary, within the scope of the current work, all energetic contributions from Gaussian curvature terms,
 256 including the boundary elements, are constant or zero and can thus be neglected. Nevertheless, in future
 257 studies where Gaussian curvature term cannot be neglected (e.g, topological changes, non-uniform saddle-
 258 splay modulus), Eq. (12) provides the geometric definition to obtain the discrete energy.

259 A numerical comparison of the discrete scalar measures with their smooth counterparts is shown in Fig. E.1.
 260 We note that for all geometric measures (i.e., volume, area, and curvatures), unlike in smooth differential geom-
 261 etry where their numerical evaluation requires the introduction of coordinates, DDG measurements are
 262 functions of mesh primitives. By substituting these discrete geometric measures from DDG into Eq. (6) and
 263 Eq. (3), we get a numerical recipe for computing the total system energy.

2.3 Force from discrete shape derivative of energy

We can obtain the force density by taking the negative shape derivative of the energy. In continuous settings, the differentiation is an infinite-dimensional problem that requires the use of the calculus of variations and differential geometry to find analytical expressions (39, 43, 70, 71) (Fig. 1E – smooth). Deriving the forces from the discrete energy (Eq. (3)) is a much simpler task.

Discrete forces can be obtained by taking partial derivatives of mesh primitives with respect to the vertex embedded coordinates, \vec{r} (Fig. 1E – discrete). Regarding notation, despite the computational differences, the differential operations in both the discrete and smooth contexts are called (discrete) shape derivatives and denoted as $\nabla_{\vec{r}}(\cdot)$ due to the common geometric meaning. We note that the computation of discrete shape derivatives for membrane modeling has been described previously in the literature (85, 87). Also that there are many overlapping definitions for discrete curvature, energy, and variations thereof in the graphics literature (105–107). Our work extends upon the prior art which evaluates derivatives algebraically, by introducing simplifications based upon the grouping of terms and identification of geometric objects. These simplifications have important implications for improving the geometric understanding as well as the run-time and numerical performance of an implementation.

At the high level, our goal is to express the forces on each vertex, given a set of physics, using geometric primitives and properties defined on specific mesh elements. By grouping terms, we find that the vertex-wise forces arising from the different physics can be expressed as weights which are functions of the input parameters and system configuration, multiplied by basic geometric vectors. We will show that these terms have an exact correspondence to terms in the smooth shape equation (Fig. 1E). We remark that, in some sense, the force expressions are reminiscent of finite difference equations which approximate differentials as a linear combination of values at discrete points. This may have implications for the suitability of modeling smooth biological surfaces with discrete meshes.

2.3.1 Force from osmotic pressure

For the smooth geometry, the shape derivative of the enclosed volume yields the outward pointing surface normal with its size equal to the local area element (108). For a discrete mesh, the shape derivative of the volume is given by the face normal on *triangular faces* with its local area element equaling to the *face area*, which is referred to as the *integrated* face normal, $\int \vec{n}_{(ijk)}$ (Fig. 1E – osmotic pressure) (87, 99, 100), where (ijk) denotes the symmetry under index permutation (e.g., $a_{i(jk)}$ means $a_{ijk} = a_{ikj}$). Similar to edge values, the force normal can be converted to vertex normal,

$$\int \vec{n}_i = \nabla_{\vec{r}_i} V = \frac{1}{3} \sum_{f_{ijk} \in N(v_i)} \int \vec{n}_{(ijk)} = \frac{1}{3} \sum_{f_{ijk} \in N(v_i)} A_{ijk} \vec{n}_{(ijk)}, \quad (14)$$

where analogous to Eq. (9), the prefactor $1/3$ accounts for fact that each face is shared by three vertices. The discrete vertex forces from the derivative of the pressure-volume work, $\int \vec{f}_i^p$, is then given by scaling it with the uniform osmotic pressure,

$$\int \vec{f}_i^p = \Delta P \int \vec{n}_i. \quad (15)$$

2.3.2 Forces from surface tension

Next considering the shape derivative of the surface energy, E_s , in smooth contexts, the derivative of the total surface area also points at the surface normal, with its magnitude measuring the size (dA) and the curvature ($2H$) of the local patch (Fig. 1E – surface tension) (108). In discrete case, we can directly compute the derivative of total area on each vertex by summing the area gradient of incident triangles with respect to the vertex position; The sum is therefore referred as (twice of) the integrated mean curvature vector on vertices,

$$\int 2\vec{H}_i = \nabla_{\vec{r}_i} A = \sum_{f_{ijk} \in N(v_i)} \nabla_{\vec{r}_i} A_{ijk} = \sum_{f_{ijk} \in N(v_i)} \int 2\vec{H}_{i(jk)}, \quad (16)$$

where we define $\int 2\vec{H}_{i(jk)} \equiv \nabla_{\vec{r}_i} A_{ijk}$, and $\int \vec{H}_{i(jk)}$ is the mean curvature vector on a triangle face corner. The capillary forces from surface tension, $\int \vec{f}_i^s$, are given by scaling the integrated mean curvature vector by the surface tension,

$$\int \vec{f}_i^s = -\lambda \int 2\vec{H}_i. \quad (17)$$

295 Evaluating the algebraic sum of area gradients reveals the “cotangent formula” applied to the vertex posi-
 296 tions (Fig. 1E – surface tension). From independent derivations with unrelated frameworks (e.g., discrete ex-
 297 terior calculus and FEM), discretizing the smooth Laplace-Beltrami operator on a triangulated mesh produces
 298 the cotangent formula which is called the discrete Laplace-Beltrami operator, $\int \Delta_s$ (99, 100, 105). Inspect-
 299 ing the expressions in Fig. 1E – surface tension, we see that our discrete expression parallels smooth theory,
 300 where the mean curvature is related to the coordinates through the application of the smooth Laplace-Beltrami
 301 operator,

$$\sum_{e_{ij} \in N(v_i)} \int 2\vec{H}_{ij} = \int \Delta_s \vec{r}_i \quad \leftrightarrow \quad \Delta_s \vec{r} = 2H\vec{n}. \quad (18)$$

302 2.3.3 Forces from bending

303 To evaluate the shape derivative of the discrete bending energy we consider the terms from the Gaussian and
 304 mean curvature separately. Based on the discrete Gauss-Bonnet theorem (Section 2.2), the total Gaussian
 305 curvature only varies if the surface undergoes a topological change. Since we do not consider non-uniform
 306 saddle-splay modulus and topological changes in the examples in this work, this term does not contribute
 307 to the force. The shape derivative of the bending energy contributed by the integrated Willmore measure
 308 requires more algebra and the introduction of halfedges, e_{ij} (c.f., Appendix C.1). Here we will focus on the
 309 key results and refer the reader to the full derivations for each term in Appendix C.2.

310 There are four fundamental geometric vectors on halfedges that comprise the bending force: the mean
 311 curvature vector (see Fig. 1B for indices),

$$\int 2\vec{H}_{ij} = \frac{1}{2} \left(\int 2\vec{H}_{i(jk)} + \int 2\vec{H}_{i(jl)} \right); \quad (19)$$

the Gaussian curvature vector,

$$\int \vec{K}_{ij} = \frac{1}{2} \varphi_{ij} \nabla_{\vec{r}_i} l_{ij}; \quad (20)$$

and the two Schafli vectors,

$$\int \vec{S}_{ij,1} = \frac{1}{2} l_{ij} \nabla_{\vec{r}_i} \varphi_{ij}, \quad \int \vec{S}_{ij,2} = \frac{1}{2} \left(l_{jk} \nabla_{\vec{r}_i} \varphi_{jk} + l_{jl} \nabla_{\vec{r}_i} \varphi_{jl} + l_{ji} \nabla_{\vec{r}_i} \varphi_{ji} \right), \quad (21)$$

312 which act to smooth the profile of local dihedral angles. Note that the shape derivatives are taken with respect
 313 to different vertices (i.e., $\nabla_{\vec{r}_i}$ or $\nabla_{\vec{r}_j}$), such that the mean curvature $\int \vec{H}_{ij}$, Gaussian curvature $\int \vec{K}_{ij}$, and
 314 Schafli vectors $\int \vec{S}_{ij}$ are asymmetric under index permutation. To account for the orientation we refer to them
 315 as *halfedge* vector quantities on e_{ij} (Appendix C.1). A numerical comparison of the discrete geometric vector
 316 with their smooth counterparts is shown in Fig. E.1 and Fig. E.2.

The bending force $\int \vec{f}_i^b$ (Fig. 1E – bending) can be expressed as weights which are functions of input parameters multiplied by basic geometric measurements in scalar and vector form,

$$\begin{aligned} \int \vec{f}_i^b = & \sum_{e_{ij} \in N(v_i)} - [\kappa_i(H_i - \bar{H}_i) + \kappa_j(H_j - \bar{H}_j)] \int \vec{K}_{ij} \\ & + \left[\frac{1}{3} \kappa_i(H_i - \bar{H}_i)(H_i + \bar{H}_i) + \frac{2}{3} \kappa_j(H_j - \bar{H}_j)(H_j + \bar{H}_j) \right] \int 2\vec{H}_{ij} \\ & - \left[\kappa_i(H_i - \bar{H}_i) \int \vec{S}_{ij,1} + \kappa_j(H_j - \bar{H}_j) \int \vec{S}_{ij,2} \right], \end{aligned} \quad (22)$$

which parallels the shape derivative of the smooth bending energy,

$$\begin{aligned}\nabla_{\vec{r}}^{\perp} E_b &= \nabla_{\vec{r}}^{\perp} \left[\int_{\mathcal{M}} \kappa (H - \bar{H})^2 dA \right] \\ &= \kappa \left[2(H - \bar{H}) (H^2 - K + \bar{H}H) + \Delta_s(H - \bar{H}) \right] dA,\end{aligned}\tag{23}$$

317 where $\nabla_{\vec{r}}^{\perp} = \nabla_{\vec{r}} \cdot \vec{n}$ is the shape derivative in the surface normal direction.

318 Comparing the smooth-discrete expressions, we make a few observations:

- 319 • The Schläfli vector terms, \vec{S} , is the discrete analog of the smooth biharmonic term, $\Delta_s(H - \bar{H})$, the high-
320 order local smoothing force. The numerical comparison of these two terms, as well as results directly
321 obtained using cotangent formula applied on pointwise scalar mean curvature, are covered in Fig. E.2
322 and Fig. E.1.
- 323 • Eq. (23) is normal component of the shape derivative of the bending energy; an additional tangential
324 component is required if surface heterogeneity exists (e.g. κ is not spatially uniform) (40, 65). In contrast,
325 the discrete shape derivative (Eq. (22)) is the total derivative in \mathbb{R}^3 , which includes both the tangential
326 and normal components⁴. Depending on the extent and symmetry of the heterogeneity, discrete force
327 can point in any direction in \mathbb{R}^3 .
- 328 • The coefficients in Eq. (22) shows an intriguing pattern combining contribution from both v_i and v_j . From
329 a finite-difference approximation standpoint, this results in an approximation scheme for which a rigorous
330 error analysis has not yet been conducted.

331 2.3.4 Net force and the benefit of DDG

332 Summing the force terms from each physics, we obtain a net force. The expression for the total force is
333 a function of geometric primitives and was derived using concepts from DDG without the need to introduce
334 coordinates and use tensor algebra. The numerical performance of these expressions are benchmarked
335 for several scalar and vector measurements on smooth and discrete surfaces shown in Fig. E.1, Fig. E.2,
336 and later discussed in Section 2.5.4. Also important, our resulting expressions allow the direct comparison
337 of terms between smooth and discrete contexts. By choosing definitions that preserve the chain of shape
338 derivatives for the geometric vectors of interest (c.f., Fig. A.2), we can preserve geometric intuition between
339 smooth and discrete differential geometry theory (100). With respect to the numerical performance, since the
340 terms of the discrete shape equation are defined using values from neighborhoods around individual vertices
341 the algorithms are efficient and straightforward to parallelize. Owing to the local nature of the force evaluation,
342 heterogeneities in material and other properties across the membrane are also straightforward to incorporate.

343 2.4 Defining metrics for simulation and error quantification

344 For monitoring simulation progress, exactness of force calculations with respect to the discrete energy, and
345 convergence studies of computed quantities upon mesh refinement we introduce the following norms.

346 2.4.1 L2 norm

347 From a PDE perspective, the vertex forces are also called the residual of the shape equation, whose solution
348 represents the equilibrium solution. The simulation is terminated when the residual is smaller than a user-
349 specified threshold. The rationale for using the L_2 norm is justified by perturbing the system configuration and
350 conducting an expansion on the system energy,

$$\begin{aligned}E(\vec{r} + \epsilon \nabla E(\vec{r})) &= E(\vec{r}) + \epsilon \langle \nabla E(\vec{r}), \nabla E(\vec{r}) \rangle + \mathcal{O}(\epsilon^2) \\ &= E(\vec{r}) + \epsilon \left\| \int \vec{f} \right\|_{L_2}^2 + \mathcal{O}(\epsilon^2),\end{aligned}\tag{24}$$

⁴In the smooth sense since there is no well-defined vertex normal direction in discrete geometry

351 where we refer the inner product of the force matrix as the L_2 norm of the forces. Computationally, this is
352 equivalent to the standard Frobenius matrix L_2 norm,

$$\left\| \int \vec{f} \right\|_{L_2} = \sqrt{\text{trace} \left(\int \vec{f}^\top \int \vec{f} \right)}. \quad (25)$$

353 Using the L_2 norm and Eq. (24), we can perform a numerical validation of the exactness of the discrete force
354 calculation with respect to the discrete energy. We expect the force to approximate the energy up to 2nd order
355 with respect to the size of a perturbation. This validation will be further elaborated in Section 3.4.

356 2.4.2 L1 norm

357 A scale-invariant L_1 norm is well-suited to quantify the magnitude of the error on varying domain size and
358 mesh resolution. Given a vertexwise local scalar measurement, $\int a$, or a vector measurement, $\int \vec{a}$, and their
359 reference values, $\int \bar{a}$, and $\int \vec{\bar{a}}$,

$$\begin{aligned} \left\| \int a \right\|_{L_1} &= \frac{\sum_{v_i} |\int a_i - \int \bar{a}_i|}{A} \\ \left\| \int \vec{a} \right\|_{L_1} &= \frac{\sum_{v_i} \|\int \vec{a}_i - \int \vec{\bar{a}}_i\|_{L_2}}{A}, \end{aligned} \quad (26)$$

360 where the normalizing factor, the total surface area A , is used to obtain a pointwise estimate of the error. The
361 L_1 norm is applied in the local comparison of discrete and smooth measurements, where we further elaborate
362 in Section 2.5.4.

363 2.5 Software implementation – Mem3DG

364 Along with the theoretical developments, we have developed an accompanying software implementation writ-
365 ten in C++ called Mem3DG. Our goal in developing this software is to enable the easy use and application of the
366 corresponding theory developed above to biological problems of interest.

367 Mem3DG is a library that contains several components to support this goal. Fig. 2 provides a synopsis of
368 Mem3DG. The input to Mem3DG includes a triangulated mesh with its coordinate \vec{r} embedded in \mathbb{R}^3 . Users can
369 choose to use Mem3DG to construct idealized meshes (e.g., icosphere, cylinder, or flat hexagonal patch) as an
370 input or to read in meshes from several common mesh formats. Meshes are stored and manipulated in Mem3DG
371 using the half-edge data structure provided by Geometry Central (109). The supported input file formats are
372 those which are readable by hapPLY and Geometry Central (109, 110). Once a mesh and parameters are
373 loaded, Mem3DG can evaluate the discrete energy and forces of the system. Mem3DG adopts a modular design
374 that facilitates the use of different energy and force components and has utilities which help the user to specify
375 the physics and governing parameters. Mem3DG also supports local system simulations where the input mesh
376 has boundaries. Additional details about the supported boundary conditions is given in Section 2.5.2.

377 To perform energy minimization and time integration of the system, various schemes have been imple-
378 mented. These schemes are described in Section 2.5.3. As discussed further in Section 2.5.4, when a user
379 wishes to use Mem3DG to represent complex biological membrane geometries, additional care regarding the
380 quality of the mesh is necessary. Mem3DG includes algorithms for basic mesh regularization and remeshing
381 which can be toggled by the user to support their applications. The simulation terminates when it reaches the
382 time limit or the system reaches equilibrium, whose criteria is determined using the energy L_2 norm introduced
383 in Section 2.4. A user can choose between several formats to output a trajectory over time or the configuration
384 of the local minima from Mem3DG. In addition to the mesh outputs supported by Geometry Central, we have also
385 developed a scheme for outputting mesh trajectories in NetCDF format (111). Mem3DG can read and visualize
386 the output trajectories and mesh configurations using Geometry Central and Polyscope (109, 112).

387 For rapid prototyping and enumeration of simulation conditions, we have also developed a Python API
388 called PyMem3DG. The functionality in C++ is exposed in Python using bindings from pybind11 (113). Illustrative
389 examples of using both Mem3DG and PyMem3DG are provided in the online tutorials. For the experiments

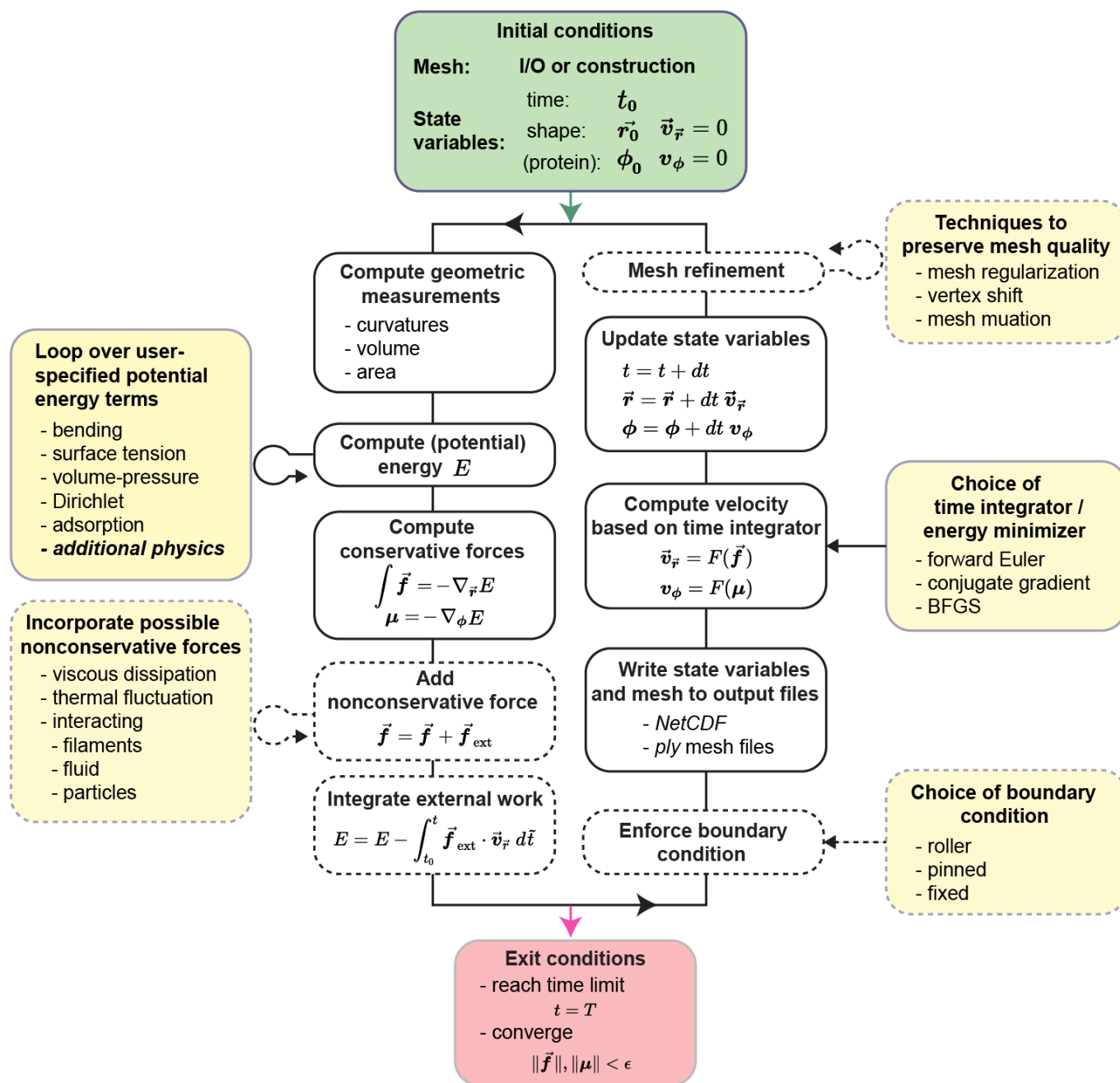


Figure 2: Overview of data flow within Mem3DG. The user provides Mem3DG with an initial condition in the form of a triangulated mesh and vertexwise state and kinematic variables (green box). The main loop (black loop) of Mem3DG evaluates the discrete energy and forces, and propagates the trajectory, among other supporting steps. Modules in dashed lines are optional depending on whether the system mesh has boundaries and if external forces are specified. User-specified options and possible extensions of Mem3DG to accommodate various physics are highlighted in yellow boxes. Mem3DG automatically exits the simulation when the system converges or the maximum time step is reached.

discussed in this work, all of the simulations were performed using PyMem3DG and the accompanying code and initial configurations are on GitHub: <https://github.com/RangamaniLabUCSD/Mem3DG>.

2.5.1 Defining properties of a membrane reservoir for systems with open boundaries

To facilitate correspondence with wet experiments and to support the reduction of computational cost, it is possible to construct systems using meshes with open-boundaries in Mem3DG. For example, when modeling the formation of a small endocytic bud from a large cell, the deformation is small compared to the broader system. If we assume that the bulk of the cell is invariant with respect to bud formation, the computational burden can be reduced by modeling only the local deformation; we can assume that the modeled patch is attached to an implicit membrane reservoir. To define this coupled system, the *constant* area (A_r) and volume (V_r) of the reservoir must also be provided. The total area and volume of the broader system is given by $A = A_{\text{patch}} + A_r$, and $V = V_{\text{patch}} + V_r$, where A_{patch} and V_{patch} are area and “enclosed volume” of the mesh patch respectively. In our models, we enforce that all elements of a boundary loop are on the same plane; this way V_{patch} can be unambiguously defined as the enclosed volume when each boundary loop is closed by a planar sheet. The capability to model systems attached to a reservoir reduces the modeled degrees of freedom while enabling intuitive physics to simplify the process of mimicking experimental conditions using Mem3DG.

2.5.2 Prescribing boundary conditions with force masking

Mem3DG supports modeling membranes with and without boundaries: a sphere (with no boundaries), a disk (with 1 boundary), and an open cylinder (with 2 boundaries). For systems without boundaries, since the force calculation of the scheme is exact, the forces will not introduce artificial rigid body motions, as was also noted by Bian *et al.* (87). To study system with boundaries, Mem3DG currently supports three types of boundary conditions:

- **Roller**, where the movement of boundary vertices is restricted along a given direction or plane.
- **Pinned**, where the position of boundary vertices are pinned while the curvature is allowed to vary.
- **Fixed**, where both the position and the boundary curvature are fixed for vertices on the boundary.

The different boundary conditions are achieved by masking the elements of the force matrix corresponding to the boundary vertices and some neighborhood. For example, to apply roller boundary conditions, we mask the Z-component of the force on the boundary vertices, therefore constraining their movement to the X–Y plane; pinned boundary conditions mask all force components for the boundary vertices to fix their position; fixed boundary conditions mask all force components for the outermost three layers to fix both their position and curvature.

2.5.3 Time integration and energy minimization

In this work, we use the forward Euler algorithm to integrate the system dynamics and the nonlinear conjugate gradient method to solve for equilibrium conditions. Both solvers are complemented by a backtracking line search algorithm, which satisfies Wolfe conditions to support adaptive time-stepping and robust minimization (114).

The forward Euler scheme was chosen as the simplest dynamical propagator; physically it represents over-damped conditions where the environment of the membrane is too viscous for the system to carry any inertia. Mathematically the physics is described by,

$$\dot{\vec{r}} = \frac{1}{\xi} \int \vec{f} = \frac{1}{\xi} \int (\vec{f}^b + \vec{f}^s + \vec{f}^p), \quad (27)$$

where ξ is the drag coefficient. From an optimization perspective, forward Euler is equivalent to the gradient descent method for minimizing an objective function, which is the discrete energy in our case.

A second propagator is the nonlinear conjugate gradient method for locally minimizing the discrete energy to yield the equilibrium shape of the membrane. Since the system is nonlinear we periodically perform

430 forward Euler (gradient descent) steps after several conjugate gradient steps. This approach of iterating be-
 431 tween conjugate gradient and gradient descent steps is commonplace in the literature for solving nonlinear
 432 systems (114).

433 We note that other time integrators and energy minimizers are also compatible with Mem3DG. Included in
 434 the software are reference implementations of Velocity Verlet integration (for symplectic time integration),
 435 and Limited-memory Broyden–Fletcher–Goldfarb–Shanno algorithm (L-BFGS, a quasi-Newton method to the
 436 equilibrium shape for large scale problems where fast computation is needed). We do not discuss these
 437 additional solvers in this work.

438 2.5.4 Practical considerations for applying Mem3DG to biological problems

439 As we have noted above, in the DDG perspective, the mesh *is* the geometry and thus the formulation of the
 440 discrete forces and energies is exact. There are therefore very few restrictions on the resolution and quality
 441 of the input mesh. However, in biophysics, we often consider biological membranes as smooth systems. We
 442 expect that many users of Mem3DG may wish to approximate a smooth system using our discrete model. In doing
 443 so, they make an implicit assumption that such an approximation is reasonable. Although the relationships
 444 between geometric objects and their shape are preserved between the smooth and discrete contexts, our
 445 ability to approximate a smooth problem with a discrete mesh is not guaranteed. Similar to finite differences
 446 and FEM, additional constraints on mesh quality and resolution must be imposed. To verify and understand
 447 the limitations of the assumption that the discrete mesh is the geometry and includes all of the geometric
 448 information, we numerically test the convergence of the discrete quantities under variation of resolution on
 449 an oblate spheroid mesh. The additional details regarding these numerical experiments are presented in
 450 Appendix D.

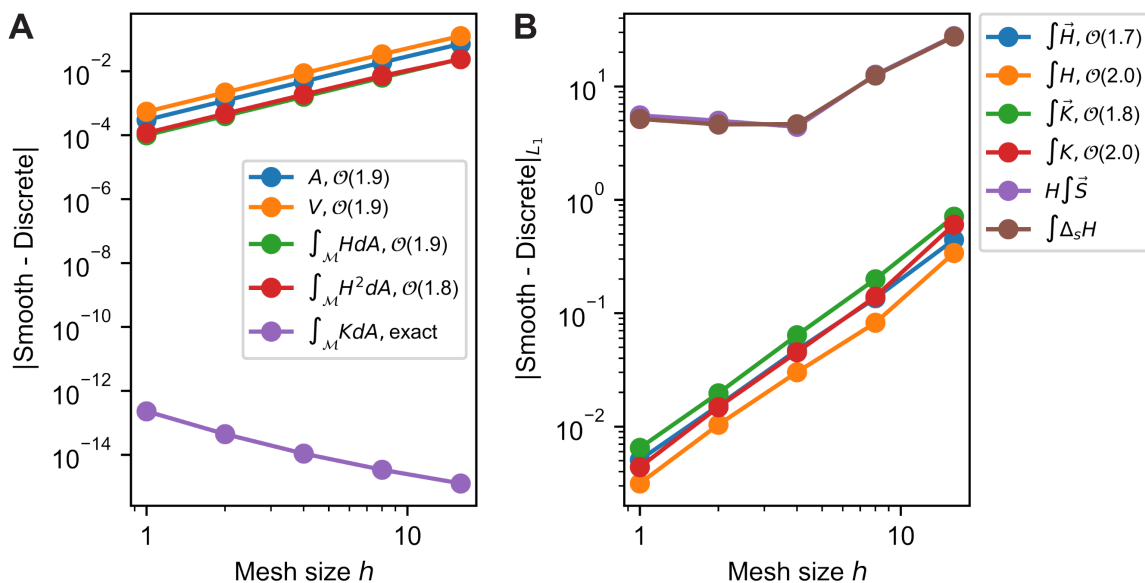


Figure 3: Comparison of discrete quantities with their smooth counterparts on spheroid shape. A) Convergence plot of global quantities, including total area, volume, mean curvature (squared), and Gaussian curvature, and B) Convergence plot of L_1 norm of scalar and vector local quantities, including the mean curvature, Gaussian curvature, and the biharmonic term.

451 Setting the characteristic length scale of the finest mesh to be $h = 1$, as the mesh coarsens (i.e., mesh
 452 size increases) h increases. Fig. 3 shows the scaling relationship of the deviation in magnitude between
 453 the smooth and discrete quantities. Fig. 3A shows the convergence property of global measurements that
 454 determines the energy (Eq. (1) and Eq. (3)), including the total area, A , enclosed volume, V , and total Gaussian
 455 curvature and mean curvature (squared), $\int_{\mathcal{M}} KdA$, $\int_{\mathcal{M}} HdA$ and $\int_{\mathcal{M}} H^2 dA$, respectively. Except for the total
 456 Gaussian curvature being an exact topological invariant, all integrated quantities exhibit approximately 2nd
 457 order convergence rate.

458 We acknowledge that convergence of global measurements does not imply that local measurements will
 459 also converge. To validate the convergence of local measurements, which determines the convergence of

460 local forces on the membrane (e.g., Eq. (15), Eq. (17) and Eq. (22)), we utilize the L_1 norm (Eq. (26)) to
461 evaluate the deviation of local quantities from their smooth counterparts. Fig. 3B shows the local convergence
462 plot. Similar to their global counterparts, local scalar mean and Gaussian curvature, $\int H$, and $\int K$, converge
463 at $\mathcal{O}(h^2)$. Fig. 3B also shows the convergence of vector quantities, which not only contribute to the magnitude
464 of the force but also set the direction of the force. The test shows that most vector quantities converge slightly
465 slower than their scalar counterparts. Two terms exhibit poor convergence, the Schläfli vector term in Eq. (22),
466 $H \int S$, and a scalar counterpart, $\int \Delta_s H$. The latter term corresponds to the direct application of the cotangent
467 Laplacian (Eq. (17)) to the pointwise scalar mean curvature field; this approach is not used in our framework
468 but is common in the literature(65). Both non-convergent expressions are discrete representations of the
469 biharmonic term, $\Delta_s H$, which have been noted to be sensitive to noise of vertex coordinates in the prior
470 literature (95). Recall that the biharmonic term is the fourth-order derivative of the embedded coordinates.
471 Although the traditional approximation theories suggest that higher-order derivatives often exhibit slower rates
472 of convergence (115), to the best of our knowledge, there is not yet a rigorous study that connects DDG
473 with an approximation theory. Nevertheless, we anticipate that similar principles hold. Two spatial plots
474 comparing local measurements between smooth and discrete contexts are provided in the appendix (Fig. E.1
475 and Fig. E.2); each test is conducted using the finest mesh size ($h = 1$). Based on this numerical validation,
476 we conclude that the computation of energy converges with a 2nd order rate (Fig. 3A). While most components
477 of the forces converge, the biharmonic term remains a limiting factor.

478 One other practical consideration for our models is that the Helfrich Hamiltonian, matching the in-plane
479 fluidity of biological membranes, has no resistance to shearing. Without additional constraints, the mesh
480 is susceptible to shearing motions which can deteriorate mesh quality in some conditions (81). This can
481 degrade the implicit assumption that the discrete mesh represents a smooth geometry. To ensure that such
482 an approximation can remain valid throughout a trajectory, we have incorporated algorithmic solutions to
483 adaptively maintain an isotropically well-resolved discrete geometry. This is achieved by two operations:
484 1) mesh regularization using local force constraints which are common in finite element methods (76, 80,
485 81, 83) Appendix E.2. and 2) mesh mutations such as decimating, flipping, and collapsing edges. Mesh
486 mutations are also a common practice to cope with deterioration in other mesh simulations which use a Monte
487 Carlo integration (60, 87–93). The algorithms for mesh regularization and mutation are further described in
488 Appendix E.

489 3 Results and Discussion

490 To further validate the method and to provide a sense of how Mem3DG can be used and extended to solve more
491 complex physics, we apply Mem3DG to a sequence of examples with increasing complexity. First, we model well-
492 studied systems with homogeneous membrane conditions. We show that Mem3DG is capable of reproducing the
493 classical solutions without imposing the axisymmetric constraint commonly adopted by other solvers. The later
494 examples set a blueprint for extending and modifying Mem3DG for particular systems of interest. We introduce
495 new energy and corresponding force terms to expand the formulation for complex systems of interest. We
496 emphasize that the goal of these examples is to illustrate the generality of the theory and software and to
497 outline specific steps for future extensions; we do not perform rigorous experimental comparisons nor extract
498 scientific insights. Additional care must be taken to mimic specific biological experiments for model validity,
499 which is left for future work.

500 Each of the following sections considers a different class of membrane biophysics problem of increasing
501 complexity in the coupling of the in-plane protein density parameter, $\phi \in [0, 1]$. To mimic the various influ-
502 ences protein-lipid interactions can have on the bilayer, the protein density can be set to influence membrane
503 properties such as the spontaneous curvature, $\bar{H}(\phi)$, and bending rigidity, $\kappa(\phi)$. More complex phenomena
504 such as the production of in-plane interfacial forces from membrane-protein phase separation(55, 59, 116)
505 can also be modeled. In our final proof of concept, we extend Mem3DG to support full mechanochemical dy-
506 namics, where proteins can mobilize in- and out-of-plane through adsorption and lateral diffusion, based on its
507 coupling with membrane material properties and shape transformation. These scenarios highlight the relative
508 ease of extending Mem3DG with additional physics and the potential utility to simulate realistic experimental

Movie 1: Animated time series simulation of Fig. 4C–reference. The color map indicates the local pointwise mean curvature, H , and t represents the numerical time. Available on GitHub: https://github.com/RangamaniLabUCSD/2020-Mem3DG-Applications/blob/master/examples/videos/compressed/pearl_control_1.mp4

Movie 2: Animated time series simulation of the unduloid shape shown in Fig. 4C–medium osmolarity. The color map indicates the local pointwise mean curvature, H , and t represents the numerical time. Available on GitHub: https://github.com/RangamaniLabUCSD/2020-Mem3DG-Applications/blob/master/examples/videos/compressed/pearl_pearl_1.mp4

509 scenarios. Note that for all of the examples, unless otherwise specified, the bending rigidity of membrane,
 510 κ , is assumed to be the rigidity of a bare membrane, $\kappa_b = 8.22 \times 10^{-5} \mu\text{m} \cdot \text{nN}$. Despite the superior perform-
 511 ance of the nonlinear conjugate gradient method in finding an energy minimizing configuration, to maintain
 512 both static and dynamic interpretability, we perform all simulations using a forward Euler integrator unless
 513 otherwise noted. All simulations presented in this work were conducted on a standard workstation with Intel
 514 Xeon processors. Although the numerical algorithms are amenable to parallelization, Mem3DG is currently a
 515 single-threaded program. Using a single core, the simulations here complete in minutes and up to two hours.

516 3.1 Modeling spherical and cylindrical membranes with homogeneous physical properties

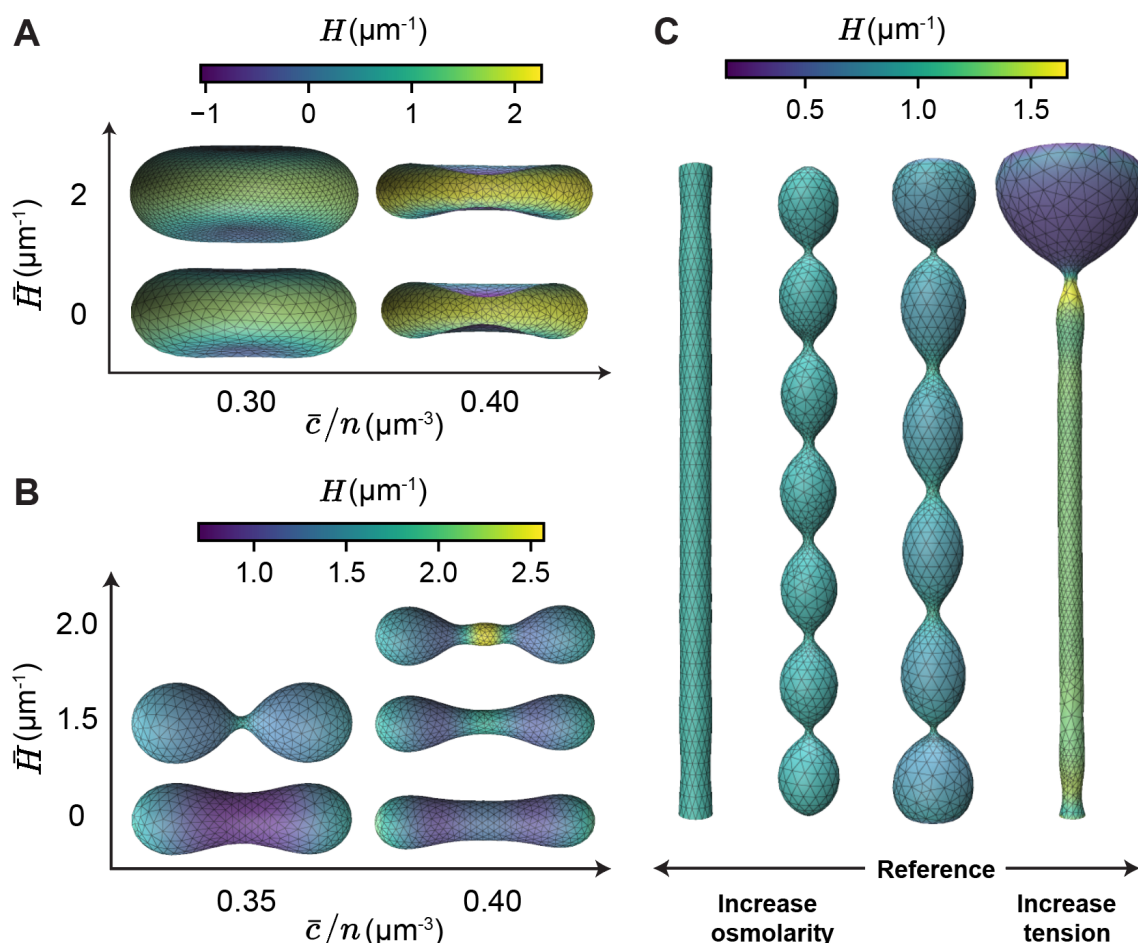


Figure 4: Recover typical equilibrium shapes of membranes with homogeneous material properties. A-B) Equilibrium solutions under different osmolarity (\bar{c}) and spontaneous curvature (\bar{H}) conditions, with initial condition of A) Oblate spheroid and B) Prolate spheroid. We vary the osmolarity by adjusting the concentration of the ambient solution, \bar{c} , while holding the enclosed amount of solute, n , constant. C) Equilibrium solutions of a tubular membrane structure under variations in osmolarity and surface tension.

517 We begin our examples by using Mem3DG to find the equilibrium shapes of membranes with homogeneous
 518 protein density, ϕ . We ask, given an initial membrane configuration with uniform bending modulus and spon-

Movie 3: Animated time series simulation of the beads-on-a-string structure shown in Fig. 4C—high tension. Disruption of the intermediate metastable state, a symmetric structure with two beads shown in Appendix A, occurs. The color map indicates the local pointwise mean curvature, H , and t represents the numerical time. Available on GitHub: https://github.com/RangamaniLabUCSD/2020-Mem3DG-Applications/blob/master/examples/videos/compressed/pearl_bead_1.mp4

519 taneous curvature, what are the minimizers of the system energy? The answers are the classical equilibrium
520 solutions to the shape equation obtained analytically (42), and numerically using many methods with differ-
521 ent assumptions (39, 117). We will show solutions obtained using Mem3DG with topologies of sphere and
522 tube (Fig. 4). These geometries were selected not only because of their potential for comparison with the
523 legacy literature but also because they are reminiscent of biological membranous structures such as red
524 blood cell (118, 119), cell-cell tunneling and tethering (120–122), neuron beading (123, 124), among other
525 biological processes.

526 Starting with closed topological spheres, Fig. 4A and B shows the typical equilibrium shapes under os-
527 motic stress while the surface area is conserved. The preferred area of the vesicle, $\bar{A} = 4\pi \mu\text{m}^2$, represents
528 a sphere of radius $1 \mu\text{m}$. This constraint is achieved by prescribing a large stretching modulus, K_A , such
529 that the areal strain, $(A - \bar{A})/A$, is less than one percent. The strength constant of osmotic pressure, K_V is
530 set to be $0.1 \mu\text{m}\cdot\text{nN}$. Initializing the simulations from an oblate spheroid, as the osmolarity increases (e.g.,
531 the normalized ambient solution, \bar{c}/n), we recover the well-known biconcave red blood cell shape (101, 117)
532 (Fig. 4A). The vesicle adopts a more convex configuration as we increase the spontaneous curvature, indi-
533 cating an overall increase in its mean curvature with the concomitant decrease of areas with negative mean
534 curvature (the dimple regions). In contrast, starting from a prolate spheroid, as the spontaneous curvature
535 increases, the vesicle adopts a dumbbell configuration as the energetically preferred state (Fig. 4B). The size
536 of the beads on the dumbbell is governed by the osmolarity, \bar{c}/n . These trends with respect to the variations
537 of the spontaneous curvature and osmolarity are consistent with the analytical and numerical results in the
538 broader literature (42, 87). Qualitatively the predicted geometries of closed vesicles with homogeneous spon-
539 taneous curvature match the predictions of a detailed benchmark of mesh-based methods performed by Bian
540 *et al.* (87).

541 We also modeled the shapes of membranes starting from an open cylinder configuration under differ-
542 ent osmotic and surface tension conditions (Fig. 4C). This problem is related to a well-studied phenomenon
543 called the Plateau-Rayleigh instability (125, 126). The Plateau-Rayleigh instability describes how surface ten-
544 sion breaks up a falling stream of fluid into liquid droplets. Compared with a liquid stream, lipid membrane
545 provides additional resistance against the instability due to its rigidity. Zhong-can and Helfrich (127) obtain
546 stability regimes as a function of membrane bending rigidity and spontaneous curvature using the spectral
547 stability analysis (127). Though osmotic pressure is often reported as an important cause of morphological
548 instability (124, 128, 129), the effect of osmotic pressure is difficult to isolate in wet experiments because
549 change to osmolarity affects the surface tension, which is a key driver of the instability. In our simulations, the
550 two effects are decoupled, making the investigation of individual contributions to the morphology possible. All
551 shapes in Fig. 4C evolve from the initial tubular mesh with radius of $1 \mu\text{m}$ and axial length of $19.9 \mu\text{m}$, under a
552 constant spontaneous curvature of $1 \mu\text{m}^{-1}$. These simulations are set up as local models (c.f., Section 2.5.1)
553 where the explicit mesh is assumed to be coupled to a membrane reservoir. Additional geometric information
554 defining the membrane reservoir and boundary conditions are required to initialize the the local model. The
555 tubular structure is considered to be a cylinder that connects two otherwise detached domains (e.g., mem-
556 brane reservoirs), which combined have a total reservoir volume, $V_r = 4.19 \mu\text{m}^3$. The strength of osmotic
557 pressure, K_V , is set to be $0.01 \mu\text{m}\cdot\text{nN}$. To isolate the effect of osmotic pressure and surface tension on the
558 morphology, we prescribe a specific surface tension which we assume to be invariant with respect to changes
559 to the surface area. On the two boundary loops of the mesh we apply roller boundary conditions, which re-
560 strict the movement of boundary vertices in the axial direction. The length of the tube is thus constrained to
561 be $19.9 \mu\text{m}$ while the radius of the tube including the boundaries is free to shrink or expand.

562 As the osmolarity increases from the reference condition ($\bar{c}/n = 0.022 \mu\text{m}^{-3}$) (Movie 1), we obtain solutions
563 such as the unduloid (or pearled) structure at $\bar{c}/n = 0.030 \mu\text{m}^{-3}$ (Movie 2), and tube at $\bar{c}/n = 0.051 \mu\text{m}^{-3}$,
564 which follow the trends from both analytical (42) and experimental observations (19, 124, 128). As we in-

565 crease the surface tension from the reference condition ($\lambda = 1 \times 10^{-7} \text{ nN} \cdot \mu\text{m}^{-1}$) to a tension-dominated
 566 regime ($\lambda = 1 \times 10^{-4} \text{ nN} \cdot \mu\text{m}^{-1}$), we obtain the beads-on-a-string structure which minimizes the surface-to-
 567 volume ratio (Movie 3). The formation of beads-on-a-string is an interesting configuration which has been
 568 identified in biological membranes and other systems (123, 124). Note that our simulations revealed a sym-
 569 metric metastable state where two large beads forms at either end (Appendix A), connected by a thin tube,
 570 prior to adopting the asymmetric conformation shown in Fig. 4C. We believe that discretization artifacts such
 571 as mesh mutations acts as a perturbation to break the symmetry of the metastable intermediate and transition
 572 the membrane to a single bead configuration.

573 These examples with uniform spontaneous curvature profile proves the ability of Mem3DG to reproduce
 574 the expected classical solutions for spherical and tubular membrane geometries. Note that no axisymmetric
 575 constraint is imposed in these simulations. Mem3DG solves the system in full three dimensions and the symmet-
 576 rical configurations is due to the problem physics. The ability to adapt changing and complex curvatures of the
 577 membrane using discrete mesh is achieved using mesh mutation and other manipulations within solver steps.
 578 For example, the pinched neck regions of the tubes are automatically decimated with finer triangles than other
 579 regions of the mesh. For a global closed membrane simulation such as in Fig. 4A, B, we do not remove any
 580 rigid body motions from the system; Since the forces from DDG are exact and we used the forward Euler
 581 integrator, no artificial rigid body motions are introduced throughout the simulation. These examples show
 582 that that the derivation of the discrete energy and forces along with the software implementation are accurate
 583 and proceed to test Mem3DG with more complex examples.

584 3.2 Modeling endocytic budding mechanisms

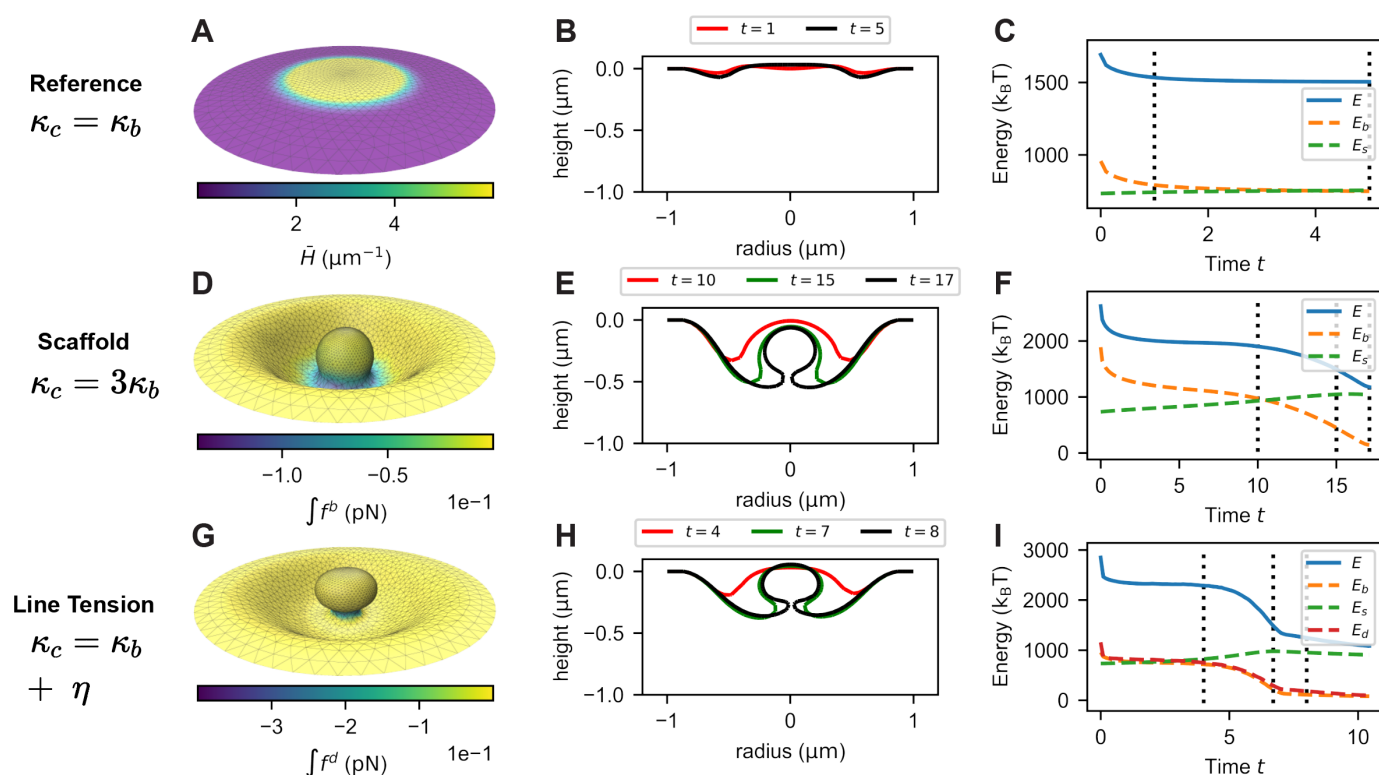


Figure 5: Budding dynamics by robust mechanisms of protein scaffolding and interfacial line tension constriction. A-C) Control group, D-F) Bending-driven scaffolding mechanism, and G-I) Interfacial line tension assisted budding. A) Spontaneous curvature distribution, \bar{H} , on initially flat patch. D) Normal projection of the bending force at $T = 15$. G) Normal projection of the line tension force at $T = 7$. B, E, H) Shape evolution through time-series snapshots of the Y-Z cross-sections of the membrane, corresponding to the vertical dash lines in C, F, I) Trajectory plots of system energy and its competing components.

585 Our goal is to highlight the potential of Mem3DG and its associated framework for investigating mechanical
 586 phenomena relevant to cellular biology. Endocytosis is a cellular process in which cells uptake cargo from
 587 the extracellular environment; the transported material is engulfed by the cell membrane which then buds

Movie 4: Animated time series simulation using the reference parameters, shown by Fig. 5A-C. The color map indicates the local point-wise spontaneous curvature and t represents the numerical time. Available on GitHub: https://github.com/RangamaniLabUCSD/2020-Mem3DG-Applications/blob/master/examples/videos/compressed/patch_control_1.mp4

Movie 5: Animated time series simulation of the bending-rigidity-driven budding, shown by Fig. 5D-F. The color map indicates the projection of the bending force onto the surface normal and t represents the numerical time. Available on GitHub: https://github.com/RangamaniLabUCSD/2020-Mem3DG-Applications/blob/master/examples/videos/compressed/patch_Kb_1.mp4

588 off to form a vesicle (13). Endocytosis occurs through various mechanisms including the clathrin-mediated
589 endocytosis (13, 130). It has been shown that clathrin aggregates on the plasma membrane helping to deform
590 the membrane and form a spherical bud (9, 13, 59). However, the specific mechanisms of how membrane-
591 clathrin interactions facilitate membrane curvature generation remains unresolved. While there is significant
592 literature investigating the many proposed mechanisms, here we develop models to demonstrate the bud
593 formation via spatially localized spontaneous curvature, combined with a line tension term arising from phase
594 separations on the membrane(131).

595 We model endocytic budding on a circular patch with radius $1\ \mu\text{m}$ (a disc with one boundary loop). We
596 assume that the patch is a *local* system which is coupled to a large vesicle (Section 2.5.1). A heterogeneous
597 protein density, $\phi \in [0, 1]$, is applied to mimic the distribution of clathrin and other scaffolding proteins. Shown
598 in Fig. 5A, the protein density is high ($\phi = 1$) towards the center of the a geodesic disk with radius $0.5\ \mu\text{m}$
599 and decreases towards the boundaries ($\phi = 0$). During simulation, the geodesic distance to the center of
600 the patch is periodically computed using the heat method (132). Vertexwise ϕ is assigned based on stair
601 step profile smoothed by the hyperbolic tangent function applied to the geodesic distance. Each experiment
602 is initialized as a flat patch and the displacement of boundary vertices are restricted using a fixed boundary
603 condition. Since the patch is viewed as a small piece within a larger closed vesicle reservoir, we assume that
604 the surface tension is constant.

605 A common model to account for the preferential bending owing to protein-membrane interactions is through
606 the spontaneous curvature; we assume $\bar{H}(\phi) = \bar{H}_c \phi$, where $\bar{H}_c = 6\ \mu\text{m}^{-1}$ is the spontaneous curvature
607 imposed by the membrane protein coat. Proteins such as clathrin are known to form stiff scaffolds on the
608 membrane. Similar to the spontaneous curvature, we can assume a linear relationship between bending
609 rigidity and protein density, $\kappa(\phi) = \kappa_b + \kappa_c \phi$, where constant κ_b is the rigidity of the bare membrane, and κ_c
610 is additional rigidity of the protein scaffold.

611 Shown in Fig. 5A-C and Movie 4, is the control simulation where we set the contribution to the rigidity
612 from protein to be the same as that of the raw membrane, $\kappa_c = \kappa_b$. Fig. 5A shows the initial flat configuration
613 of the control experiment; the color bar shows the heterogeneous spontaneous curvature resulted from the
614 prescribed protein density profile. In the control experiment, the bending force is resisted by the surface tension
615 (Fig. 5C) until, at the final frame in Fig. 5B ($t = 5$), the membrane reaches the equilibrium configuration where
616 the surface tension cancels with the bending force. In a second model, we assume that the scaffolding proteins
617 is much more rigid than the bare membrane, $\kappa_c = 3\kappa_b$. Fig. 5D-F and Movie 5 show the bud formation due to
618 this increased protein scaffolding effect. The greater rigidity results in an increase of initial bending energy,
619 which outcompetes the resistance from the surface tension (Fig. 5F). Fig. 5E shows the shape evolution from
620 a flat patch to a successful bud with pinched neck. Fig. 5D shows the signed projection of the bending force
621 onto the vertex normal, $\int f_i^b = \int \bar{f}_i^b \cdot \bar{n}_i$, at $T = 15$.⁵ We can see an “effective line tension” driven by the
622 heterogeneous spontaneous curvature which constricts the neck. This phenomenon is theoretically explored
623 in detail by Alimohamadi *et al.* (58).

624 For our third model, based on the prior observations that protein phase separation on surfaces can lead

⁵Outward-pointing angle-weighted normal; the same applies to the interfacial line tension.

Movie 6: Animated time series simulation of budding driven by interfacial line tension, shown by Fig. 5G-I. The color map indicates the signed projection of the line tension force onto the surface normal and t represents the numerical time. Available on GitHub: https://github.com/RangamaniLabUCSD/2020-Mem3DG-Applications/blob/master/examples/videos/compressed/patch_eta_1.mp4

Movie 7: Animated time series simulation of protein aggregation on a dendritic spine (Fig. 6B). The color map shows the order parameter for protein density, $\phi \in (0, 1)$, and t represents the numerical time. Available on GitHub: https://github.com/RangamaniLabUCSD/2020-Mem3DG-Applications/blob/master/examples/videos/compressed/spine_1.mp4

625 to a line tension (131), we incorporate a Ginzburg-Landau interfacial energy into the system,

$$E_d = \frac{1}{2} \sum_{f_{ijk}} \eta \int \|\nabla_{\vec{\theta}} \phi\|_{ijk}^2 \rightarrow \frac{1}{2} \int_{\mathcal{M}} \eta \|\nabla_{\vec{\theta}} \phi\|^2 dA. \quad (28)$$

626 where η , referred to as the Dirichlet energy constant, governs the strength of the energy penalty, and $\nabla_{\vec{\theta}} \phi$ is
 627 the discrete surface gradient of protein density profile. The term is similar to previous modelling efforts by Elliott
 628 and Stinner (78) and Ma and Klug (77) using FEM; because we use the protein phase separation as a prior,
 629 we exclude the double-well term which models the thermodynamics of phase-separation, and incorporate only
 630 the Dirichlet energy component that penalizes the heterogeneity of membrane composition.

Defined as the slope of the linearly interpolation of ϕ on faces of the mesh, f_{ijk} , the discrete surface gradient of the protein density is,

$$\nabla_{\vec{\theta}} \phi_i = \frac{1}{2A_{ijk}} \sum_{\underline{e}_i \in N(f_{ijk})} \phi_i \underline{e}_i^{\perp}, \quad (29)$$

631 where following illustration in Fig. 1C, \underline{e}_i is the vector aligned with the halfedge \underline{e}_i , with its length of l_i , and $(\cdot)^{\perp}$
 632 represents a 90° counterclockwise rotation in the plane of f_{ijk} . The resulting line tension force $\int \vec{f}^d$ is then the
 633 shape derivative of the Dirichlet energy, $\nabla_{\vec{r}} E_d$, which acts to minimize the region with sharp heterogeneity.
 634 The detailed derivation of the shape derivative is elaborated in Appendix C.3, where we follow the formulaic
 635 approach by taking geometric derivatives of basic mesh primitives shown in Eq. (49). Fig. 5G-I and Movie 6
 636 show the trajectory where we used control bending rigidity, $\kappa_c = \kappa_b$, and the additional interfacial line tension,
 637 $\eta = 5 \times 10^{-4} \mu\text{m} \cdot \text{nN}$. We find that the interfacial line tension, jointly with the bending force, lowers the system
 638 energy and help the formation of a spherical bud (Fig. 5I, H). Fig. 5G shows the snapshot ($t = 7$) with the
 639 color map representing the signed normal projection of the interfacial line tension that acts to constrict the
 640 neck. These examples of endocytic bud formation help to illustrate the utility of Mem3DG and the accompanying
 641 theoretical framework. Since physical parameters are assigned on a per-vertex basis, it is straightforward
 642 to incorporate heterogeneity such as the nonuniform bending rigidity and spontaneous curvature. In smooth
 643 theory and its derived discrete mesh models, when membrane is heterogeneous, it is required to decompose
 644 the force separately in normal and tangential direction (40, 65); In contrast, the general derivation of the dis-
 645 crete bending force following the formalism of DDG permits modeling membrane with heterogeneous material
 646 properties without any modification to its formulation (Section 2.3.3). The introduction of Dirichlet energy and
 647 line tension force serves to highlight the relative ease to extend the modelled physics.

648 3.3 Protein aggregation on the realistic mesh of a dendritic spine

Table 3: Parameters used in Section 3.3

Parameters	Values
ϕ_0	0.1
κ_c	0 nN· μm
\bar{H}_c	10 μm^{-1}
B	3 nN $^{-1}$ · μm^{-1} ·s $^{-1}$
η	0.01 μm ·nN

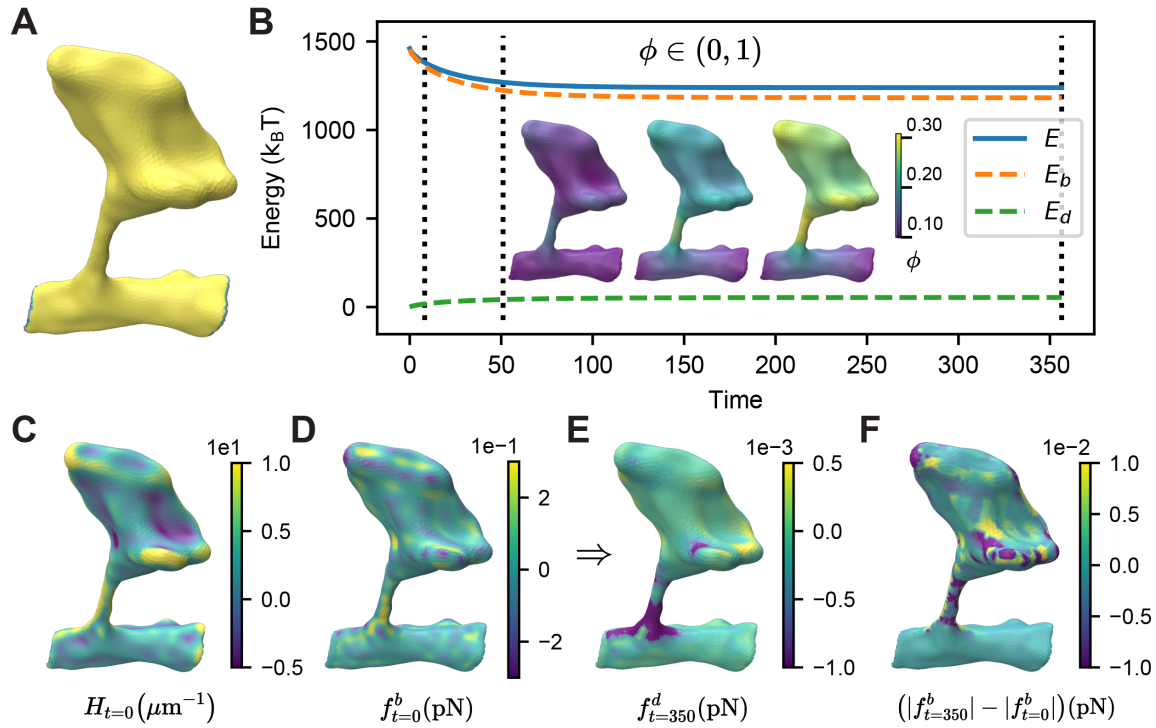


Figure 6: Protein aggregation on a realistic dendritic spine geometry. A) Mesh of the dendritic spine and its boundary elements. B) Trajectory of protein evolution and components of system energy. C) Mean curvature of the geometry. The normal component of D) the bending force at $t = 0$, E) the line tension force produced by the equilibrium protein distribution, and F) the difference in the bending force profile produced by final protein distribution as opposed to the initial distribution.

649 While the prior examples have focused on the mechanical response of the membrane given a bound
 650 protein distribution, we can also model the inverse problem. Given the membrane shape, how do curvature-
 651 sensing proteins diffuse in the plane of the membrane and distribute over the domain? And how does
 652 the resultant protein distribution influence the stresses of the system? To model the protein dynamics, we use
 653 three terms corresponding to protein binding, curvature sensitivity, and lateral diffusion.

654 To model the binding of proteins to the membrane, we assume that the energy of adsorption, ε , is constant
 655 and uniform across the surface such that the discrete adsorption energy is,

$$E_a = \varepsilon \sum_i \int \phi_i, \quad (30)$$

656 where ϕ_i is an order parameter representing the area density of protein at each vertex. Taking the derivative
 657 with respect to ϕ , referred to as the chemical derivative,

$$\mu_i^a = -\nabla_\phi E_a = -\int \varepsilon, \quad (31)$$

658 we obtain the adsorption component of the chemical potential. To account for protein curvature-sensitivity,
 659 we find the chemical potential of the bending energy,

$$\mu_i^b = -\nabla_\phi E_b = \int [2\kappa_i(H_i - \bar{H}_i)\nabla_\phi \bar{H}_i - (H_i - \bar{H}_i)^2 \nabla_\phi \kappa_i], \quad (32)$$

660 where we assume that $\nabla_\phi \kappa_i = \kappa_c$, and $\nabla_\phi \bar{H}_i = \bar{H}_c$ where κ_c and \bar{H}_c are constant parameters defined in
 661 Section 3.2. The first term of Eq. (32) is the shape mismatch penalty; considering the binding of a rigid protein
 662 which induces a significant spontaneous curvature change, if the curvature of membrane is far from this new
 663 spontaneous curvature, then the shape mismatch between the membrane and proteins will prevent binding.
 664 Alternatively, if the protein is more flexible, a shape mismatch results in a small energetic penalty. The second
 665 term of Eq. (32) endows the protein with curvature sensitive binding.

666 The in-plane diffusion of the protein is accounted for by the chemical derivative of the smoothing Dirichlet
667 energy, E_d ,

$$\mu_i^d = -\nabla_\phi E_d = -\int \eta \Delta_s \phi_i, \quad (33)$$

668 where η is the same Dirichlet energy constant introduced in Eq. (28). The total chemical potential captures
669 the bending, adsorption and diffusion components. A mobility rate constant, B , determines the time scale of
670 the chemical response,

$$\dot{\phi} = B\mu = B(\mu_b + \mu_a + \mu_d). \quad (34)$$

671 We investigate the influence of curvature dependent binding to a realistic dendritic spine geometry which
672 was reconstructed from electron micrographs and curated using GAMer 2 (Fig. 6A) (32). The mean curvature
673 of the spine geometry is shown Fig. 6C. We isolate the effect of curvature-dependent binding by assuming
674 that the shape of the spine is fixed and impose Dirichlet boundary conditions at the base on the spine to fix
675 the protein concentration, $\phi = 0.1$ (Fig. 6A).

676 Starting from a homogeneous protein distribution, $\phi_0 = 0.1$, Fig. 6B and Movie 7 show the evolution of
677 the protein distribution and a trajectory of the system energy. Note that for simplicity, we have turned off the
678 adsorption energy term since it only shifts the basal protein-membrane interactions which will also be set by the
679 Dirichlet boundary condition. Mem3DG constrains the range of $\phi \in (0, 1)$ using the interior point method (114).
680 Due to the curvature sensitivity of the protein, illustrated by the snapshots (Fig. 6B, $T = 350$) representing the
681 final protein distribution, the protein aggregates towards regions of high curvature (e.g., on the spine head).

682 Although the proteins can reduce the bending energy by modulating the local bending modulus and spon-
683 taneous curvature, the protein distribution at equilibrium does not cancel out the bending energy. We expect
684 that the Dirichlet energy term, which limits ϕ to be smooth across the geometry, restricts the protein from further
685 aggregating to the extent required to cancel out the bending energy. The components of forces on the initial
686 and final configurations of the spine are compared in Fig. 6D-F. The initial homogeneous protein distribution
687 has no line tension forces and a bending force shown in Fig. 6D. After the protein distribution reaches steady
688 state, line tension appears in response to membrane heterogeneity Fig. 6E. We hypothesize that, similar to
689 Section 3.2, the line tension constricts the neck of the spine and helps to support the cup-like structures in the
690 spine head. While in most regions the distribution of proteins reduces the force, several regions experience
691 increased stress Fig. 6F. Note that the magnitude of the forces generated by proteins in this model are orders
692 of magnitude smaller than the initial bending force. Thus, this example demonstrates that Mem3DG can be used
693 on meshes imported from realistic geometries of cellular substructures.

694 3.4 Membrane dynamics with full mechanochemical feedback

Table 4: Parameters used in Section 3.4 for models with full mechanochemical feedback

Parameters	Values
ϕ_0	0.1
κ_c	0 nN· μm
\bar{H}_c	10 μm^{-1}
K_V	0.5 nN· μm
K_A	1 nN· μm^{-1}
B	3 nN $^{-1}$ · μm^{-1} ·s $^{-1}$
ε	-1×10^{-3} nN· μm
η	0.1 μm ·nN
\bar{V}	2.91, 3.95, 4.99 μm^3

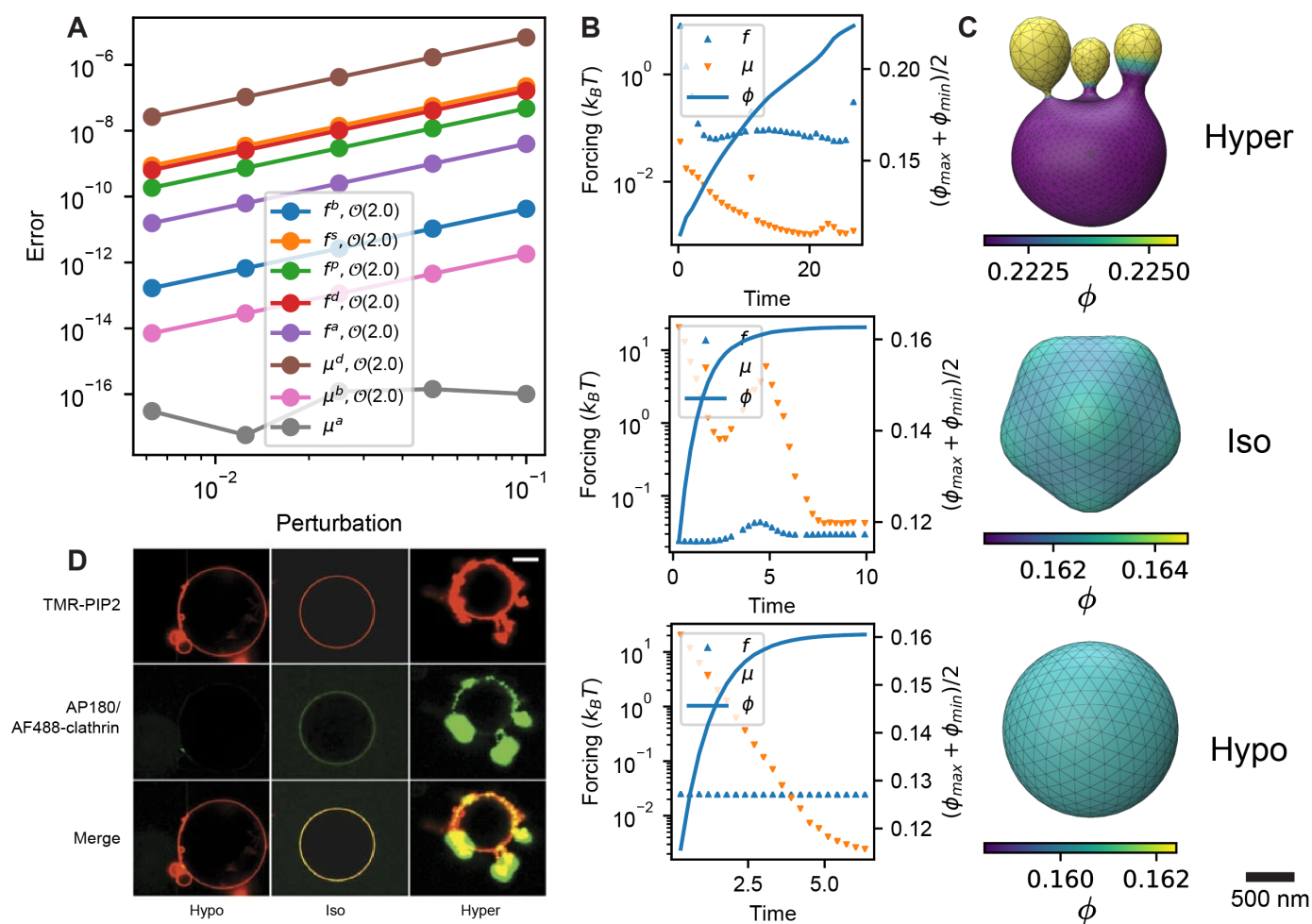


Figure 7: Modeling budding from a vesicle driven by the full mechanochemical feedback of membrane-protein interactions. A) Validation of the exactness of the discrete forcing with respect to the discrete energy. The terms correspond to forces from bending f_b , tension-area f_s , pressure-volume f_p , Dirichlet f_d , and protein binding f_a . μ_d , μ_b , and μ_a are the chemical potential of diffusion, bending, and binding respectively. B) The time trajectory of budding dynamics in hypertonic, isotonic, and hypotonic osmotic condition. C) The final snapshot of the system configuration under hypertonic, isotonic, hypotonic condition. D) Similar geometries to those shown in C) have been observed in experiments by Saleem *et al.* (59).

Movie 8: Animated time series simulation of the hypertonic case shown in Fig. 7B-C. The color map shows the order parameter for protein density, $\phi \in (0, 1)$, and t represents the numerical time. Available on GitHub: https://github.com/RangamaniLabUCSD/2020-Mem3DG-Applications/blob/master/examples/videos/compressed/bud_hyper_1.mp4

Movie 9: Animated time series simulation of the isotonic case shown in Fig. 7B-C. The color map shows the order parameter for protein density, $\phi \in (0, 1)$, and t represents the numerical time. Available on GitHub: https://github.com/RangamaniLabUCSD/2020-Mem3DG-Applications/blob/master/examples/videos/compressed/bud_iso_1.mp4

695 In this section, we will demonstrate the use of Mem3DG to model the complete mechanochemical feedback of
696 a protein-membrane system. For the following simulations, not only can proteins bind in a curvature-dependent
697 manner, the membrane can also deform leading to a feedback loop. We have introduced all of the force terms
698 in previous sections except the shape derivative of the adsorption energy,

$$\int \vec{f}_i^a = -\nabla_{\vec{r}} E_a = -2\varepsilon \phi_i \int \vec{H}_i, \quad (35)$$

699 which accounts for the change in the area of protein coverage (i.e., expanded coverage if $\varepsilon < 0$).

700 Revisiting the claim that all discrete forcing is exact with respect to the discrete energy, we validate by
701 examining the convergence of the forcing terms with respect to the size of perturbation to the system con-
702 figuration, ϵ (Fig. 7A). This is based on the leading order expansion done in Eq. (24), which concludes that
703 the forcing terms are exact if their rate of convergence is at least 2nd order. Shown in Fig. 7A, this is true for
704 all forcing terms; note that since the adsorption energy, E_a , is a linear function with respect to ϕ , μ^a can be
705 determined to the machine precision for all perturbation sizes. A meaningful discrete-smooth comparison of
706 all terms in the energy and forcing similar to Section 2.5.4 requires the analytical solutions of the bending force
707 and interfacial line tension arising from the spatially heterogeneous membrane properties, which to the best
708 of our knowledge, are not available. In Section 3.2, we introduced a heterogeneous membrane composition
709 as a static property. By prescribing the protein density profile, we are able to get hints about how to form
710 membrane buds from a patch. Here we lift this assumption and simulate the dynamics of osmotic pressure-
711 driven budding from a vesicle. The dynamics couples the protein-membrane mechanochemical feedback and
712 includes protein binding and diffusion introduced in Section 3.3. The expressions of discrete free energy and
713 forcings do not change but we allow the membrane configuration and protein density to interact and evolve
714 simultaneously.

715 We start each simulation from a sphere with a uniform protein concentration, $\varphi = \varphi_0 = 0.1$. We consider
716 the evolution of the system in different osmotic conditions: hyper-, iso-, and hypotonic. Additional parameters
717 for these simulations are given in Table 4. Fig. 7B shows plots of the mechanical, $\|\vec{f}\|_{L_2}^2$, and chemical re-
718 sponse, $\|\mu\|_{L_2}^2$, along with the protein density, $(\phi_{\max} + \phi_{\min})/2$, over the trajectory for each osmotic condition.
719 Note that under hypo- and isotonic conditions, the system reaches (quasi) steady state where both the shape
720 and protein distribution stabilize, while in hypertonic solution, the system continues to experience strong me-
721 chanical force and protein mobility, which we expect to drive further morphological changes of the membrane
722 beyond our simulation stopping point. Fig. 7C shows the final snapshot of each simulation across the os-
723 motic conditions with the protein density represented by the color map. In hypertonic conditions, the osmotic
724 pressure provides sufficient perturbations to membrane morphology, which initializes the positive feedback
725 loop between membrane curvature generation and protein aggregation; This mechanochemical feedback
726 jointly promotes the outward bending of the membrane and results in the bud formation (Fig. 7C–hyper and
727 Movie 8). Under isotonic and hypotonic conditions, the osmolarity does not permit the large change in volume
728 required to form spherical buds with small neck radius. In hypotonic condition, the pressure-tension balance
729 provides substantial stability to the initial spherical configuration. In comparison, in the isotonic condition, the
730 comparable competition between the chemical and mechanical response leads to a patterned protein distri-
731 bution and an undulating morphology (Fig. 7C–hypo and Movie 9). This example illustrates the possibility to
732 utilize Mem3DG to model a full mechanochemical feedback between membrane and protein. Although we do not
733 intend to replicate the exact experimental conditions and assumptions, the geometries obtained from these
734 simulations resemble the shapes obtained by Saleem *et al.* (59) who investigated budding from spherical
735 vesicles under differing osmotic conditions (Fig. 7D) (59).

736 4 Summary

737 In this work, we introduce a new perspective for constructing a 3D membrane mechanics model on discrete
738 meshes. The goal of our approach is to close the gap between existing discrete mesh based models(60,
739 84–94, 97, 98) and the smooth theory. Specifically, we seek to advance the discussion behind the choice of
740 algorithmic approaches for computing geometric values required for the discrete energy and force (65, 87,

741 **95**). We start by writing a discrete energy, Eq. (3), mirroring the spontaneous curvature model. Then using
742 the perspective of DDG, we show that there is a formulaic approach for deriving the corresponding discrete
743 force terms based on fundamental geometric vectors. By identifying geometric invariants and grouping terms,
744 the resulting discrete forces have exact correspondence to the traditional smooth theory. This helps us to
745 facilitate the comparison between smooth and discrete contexts enabling new geometric perspectives and
746 understanding of numerical accuracy. Moreover, the discrete force terms are functions of readily accessible
747 geometric primitives, and the formulation is amenable for efficient implementation and extension.

748 We have produced a reference software implementation called Mem3DG. Using Mem3DG, we validate our theory
749 by reproducing the solutions to the classical shape transformations of a spherical and tubular vesicle. We
750 further demonstrate the derivation and incorporation of additional physics terms to model protein-membrane
751 interactions. Following our formulaic approach using DDG, we derived the discrete analog of various physics
752 such as the interfacial line tension, surface-bulk adsorption, protein lateral diffusion, and curvature-dependent
753 protein aggregation. To exemplify all the introduced physics, the full mechanochemical coupling between the
754 membrane shape and protein density evolution results in protein localization, pattern formation, and budding.
755 These examples serve to highlight the extensibility of the framework, which does not require the introduction
756 of coordinates and advanced tensor calculus commonly needed to solve problems on arbitrary manifolds.
757 The software implementation Mem3DG was designed to facilitate coordination between theoretical modeling
758 and wet-experiments; and we hope to support the modeling of scenes with well resolved protein-membrane
759 interactions such as in the electron tomograms (133). We expect that as the advances in biophysical modeling
760 and membrane ultrastructure imaging progresses, Mem3DG will emerge as a useful tool to test new hypothesis
761 and understand cellular mechanobiology.

762 **5 Acknowledgments**

763 The authors would like to acknowledge Dr. Ali Behzadan, Prof. Ravi Ramamoorthi, and Prof. Albert Chern for
764 helpful discussions and critical feedback. This work was supported in part by the National Institutes of Health
765 R01GM132106, National Science Foundation DMS 1934411, and an Air Force Office of Scientific Research
766 DURIP FA9550-19-1-0181 to PR. CTL also acknowledges support from a Hartwell Foundation Postdoctoral
767 Fellowship.

768 Appendices

769 A Supplemental figures

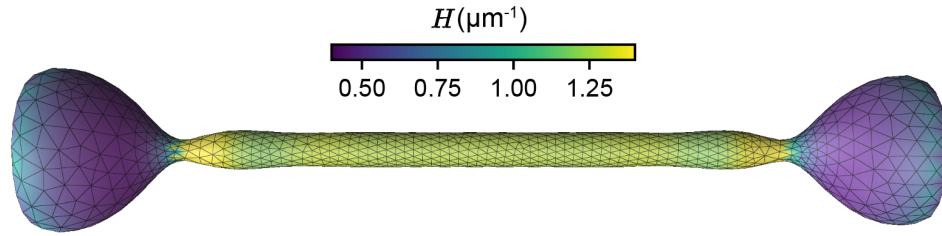


Figure A.1: A symmetric metastable state with two beads instead of single larger bead is observed, prior to collapsing to the solution shown in Fig. 4C – high tension

Smooth	↔	Discrete
$\nabla_{\vec{r}} \left(\begin{array}{l} \text{vol}(\mathcal{M}) = \frac{1}{3} \int_{\mathcal{M}} \vec{n} \cdot \vec{r} \, dA \\ \vec{n} \, dA \end{array} \right)$		$\nabla_{\vec{r}} \left(\begin{array}{l} \sum_{f_{ijk}} V_{0ijk} \\ \int \vec{n}_i = \frac{1}{3} \sum_{f_{ijk} \in N(v_i)} \int \vec{n}_{(ijk)} = \frac{1}{3} \sum_{f_{ijk} \in N(v_i)} A_{ijk} \vec{n}_{(ijk)} \end{array} \right)$
$\nabla_{\vec{r}} \left(\begin{array}{l} \text{Area}(\mathcal{M}) = \int_{\mathcal{M}} dA \\ 2H\vec{n} \, dA \end{array} \right)$		$\nabla_{\vec{r}} \left(\begin{array}{l} \sum_{f_{ijk}} A_{ijk} \\ \int 2\vec{H}_i = \sum_{e_{ij} \in N(v_i)} \int 2\vec{H}_{ij} = \frac{1}{2} \sum_{e_{ij} \in N(v_i)} (\cot \angle_{ikj} + \cot \angle_{ilj}) \vec{e}_{ji} \end{array} \right)$
$\nabla_{\vec{r}} \left(\begin{array}{l} \text{Mean}(\mathcal{M}) = \int_{\mathcal{M}} H \, dA \\ \text{Assume closed} \\ K\vec{n} \, dA \end{array} \right)$		$\nabla_{\vec{r}} \left(\begin{array}{l} \sum_{e_{ij}} \int H_{ij} = \frac{1}{2} \sum_{e_{ij}} l_{ij} \varphi_{ij} \\ \text{Assume closed} \\ \int \vec{K}_i = \sum_{e_{ij} \in N(v_i)} \int \vec{K}_{ij} = \frac{1}{2} \sum_{e_{ij} \in N(v_i)} \frac{\varphi_{ij}}{l_{ij}} \vec{e}_{ji} \end{array} \right)$
$\nabla_{\vec{r}} \left(\begin{array}{l} \text{Gauss}(\mathcal{M}) = \int_{\mathcal{M}} K \, dA \\ \text{Gauss-Bonnet} \\ 0 \end{array} \right)$		$\nabla_{\vec{r}} \left(\begin{array}{l} \sum_{v_i} \int K_i = \sum_{v_i} \left(2\pi - \sum_{f_{ijk} \in v_i} \angle_{jik} \right) \\ \text{Gauss-Bonnet} \\ 0 \end{array} \right)$

Figure A.2: Steiner's formula in continuous and discrete geometry: chain of smooth and discrete shape derivatives of integrated geometric measurements.

770 B Rationale for integrated measures in discrete contexts

771 The rationale for why an integrated measurement in discrete contexts is the natural counterpart to pointwise
 772 measures in smooth contexts can be demonstrated by considering the curvature of a discrete polygonal curve.
 773 If we attempt to define the curvature, C , of the discrete polygonal curve in a naïve pointwise manner, following
 774 the procedure in smooth settings, we will find zero curvature along edges and infinite curvature (owing to

775 the discontinuity) on vertices. Thus the traditional view of curvature from smooth manifolds reveals no useful
776 information about the geometry of the discrete curve. We must find another geometric relationships which can
777 translate between smooth and discrete contexts to maintain the geometric connection.

778 One candidate relationship from differential geometry for smooth objects, is the equivalence of the inte-
779 grated curvature and the turning angle ψ (i.e., the total angle by which the tangent vector of the curve turns
780 over some domain l). Returning to the discrete context, we can seek to preserve this relationship between
781 the integrated curvature and turning angle by finding a compatible definition. Since the discrete turning angle,
782 ψ_i , between two connected edges of the discrete polygonal curve is well-defined, we can set the “discrete”
783 curvature, $\int C$, of a vertex, v_i , to be

$$\left(\int C\right)_i \equiv \psi_i. \quad (36)$$

784 We note that the notation for the discrete curvature, $\left(\int C\right)_i$ is used only in this illustrative example; in the
785 remainder of the text, we will omit the parenthesis and use the simplified notation, $\int C_i$. To make sense of the
786 integral over a discrete object, additional care must be taken to represent the curvature from a distributional
787 sense (99). This is related to traditional approximation methods, such as the point allocation method, which
788 bridges a smooth and discrete problem by convoluting the smooth problem with impulse functions (e.g., the
789 Dirac delta function) at a finite number of locations (115).

790 As we have shown, integrated geometric measurements enable us to preserve geometric relationships
791 (from smooth contexts) for discrete objects, and are thus preferred over pointwise definitions. Nevertheless,
792 we often require a pointwise discrete measurement for use in algorithms and visualization. An integrated
793 measurement can be converted to a meaningful pointwise discrete measurement by normalizing the value
794 over a domain. For the discrete polygonal curve, the domain can be the dual vertex length, l_i (i.e., the discrete
795 analog of l). l_i is given by half of the sum lengths of the two incident edges. A pointwise curvature on the
796 vertex v_i is then given by,

$$C_i = \int C_i/l_i = \psi_i/l_i. \quad (37)$$

797 Another rationale for using an integrated value for a discrete geometric measurement, is that we can arrive
798 at the same definition from multiple perspectives. Returning to the definition of the curvature of a polygonal
799 curve, without introducing the turning angle, we can arrive at the same result by adopting the Steiner view
800 (99, 134)⁶. In the Steiner view, we replace the sharp vertices with a smooth circular arc with radius ϵ such that
801 the discrete geometry is made smooth such that the curvature is well-defined everywhere. As the only curved
802 section, every circular arc has a discrete (integrated) curvature,

$$\int C = \int_{\text{arc}} C ds = C_{\text{arc}} l_{\text{arc}} = \frac{1}{\epsilon}(\epsilon\psi) = \psi, \quad (38)$$

803 where $C_{\text{arc}} = 1/\epsilon$ is the curvature of the circular arc, and $l_{\text{arc}} = \epsilon\psi$ is the arc length. We see that in the Steiner
804 view, the integrated curvature is still equivalent to the turning angle. Following similar logic, other discrete
805 definitions are described in Section 2.2 and the DDG literature (99, 100).

806 C Discrete shape and chemical derivatives of discrete energy

807 C.1 Halfedge on a triangulated mesh

808 A scalar measure on an edge is symmetric with respect to index permutation; For example, the scalar mean
809 curvature (Eq. (8)),

$$\int H_{ij} = \int H_{ji} = \frac{l_{ij}\varphi_{ij}}{2}. \quad (39)$$

⁶We will use the Steiner view to define the discrete curvature of a surface in Section 2.2

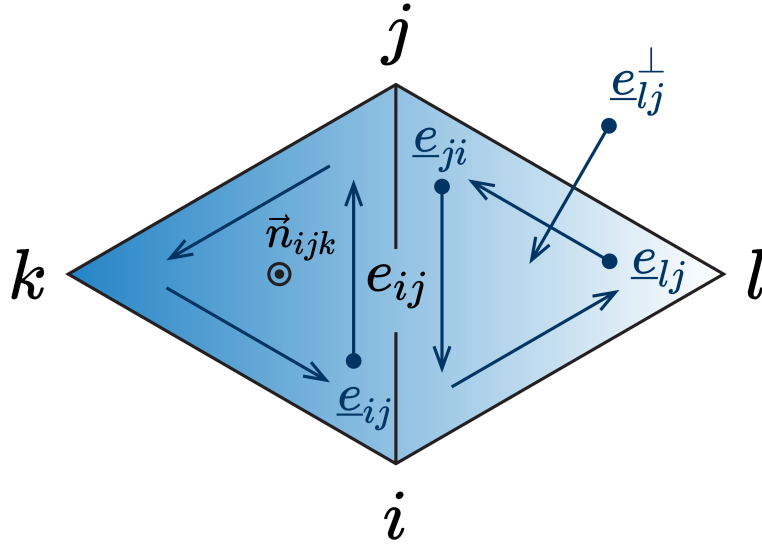


Figure C.1: Schematics for halfedge on a triangulated mesh.

810 However, as we will show in detail in the following sections, this symmetry does not apply to vector measures,
 811 which compose the discrete shape derivative of the energy. For example, the corresponding mean curvature
 812 vector,

$$\int \vec{H}_{ij} \neq \int \vec{H}_{ji}. \quad (40)$$

813 To highlight the directionality of vector quantities and disambiguate the notation, here we review the concept
 814 of halfedge on a triangulated mesh. Given any non-boundary edge, e_{ij} , on a manifold mesh, there exists
 815 two associated halfedges, e_{ij} and e_{ji} (Fig. C.1). This convention leads to an oriented (counterclockwise)
 816 halfedge loop on each triangle face and subsequently a well-defined 1) 90° counterclockwise rotation of the
 817 halfedge in the plane of the face (e.g., $e_{lj} \rightarrow e_{lj}^\perp$), and 2) face normal (outward) based on the right hand
 818 rule Fig. C.1. Beside being able to differentiate vector/scalar measures, the concept of halfedge is widely
 819 adopted data structure for managing connected graph, or meshes, for which we refer the reader to the broader
 820 literature (109, 135).

821 C.2 Deriving the bending force as the shape derivative of bending energy

The geometric derivatives of mesh primitives, including edge length, l , dihedral angle, φ , vertex dual area, A ,
 are given as

$$\nabla_{\vec{r}_i} l_{ij} = \frac{\vec{e}_{ji}}{l_{ij}}, \quad (41a)$$

$$\nabla_{\vec{r}_i} \varphi_{ij} = \frac{1}{l_{ij}} (\cot \angle_{ijk} \vec{n}_{ijk} + \cot \angle_{ijl} \vec{n}_{ilj}), \quad (41b)$$

$$\nabla_{\vec{r}_i} \varphi_{jk} = -\frac{1}{l_{jk}} (\cot \angle_{ijk} + \cot \angle_{ikj}) \vec{n}_{ijk} = -\frac{l_{jk}}{2A_{ijk}} \vec{n}_{ijk}, \quad (41c)$$

$$\nabla_{\vec{r}_i} A_i = \frac{1}{3} \sum_{f_{ijk} \in N(v_i)} \nabla_{\vec{r}_i} A_{ijk} = \frac{1}{6} \sum_{e_{ij} \in N(v_i)} (\cot \angle_{ikj} + \cot \angle_{ilj}) \vec{e}_{ji}, \quad (41d)$$

$$\nabla_{\vec{r}_i} A_j = \frac{1}{3} \sum_{f_{ijk} \in N(e_{ij})} \nabla_{\vec{r}_i} A_{ijk} = \frac{1}{6} (\vec{e}_{jk}^\perp + \vec{e}_{lj}^\perp), \quad (41e)$$

822 where \vec{n}_{ijk} is the unit normal vector of the face f_{ijk} , \vec{e}_{ji} is the vector aligned with the halfedge, e_{ji} , with its
 823 length of l_{ij} . The indices and nomenclature in Eq. (41b), Eq. (41c) and Eq. (41e) are illustrated in the diamond
 824 neighborhood (Fig. C.1) and those of Eq. (41d) are illustrated in the fan neighborhood (Fig. 1A).

To simplify the expression and provide more structure for the subsequent discrete variation, it is convenient to define some fundamental curvature vectors,

$$\int 2\vec{H}_{ij} = \frac{1}{2}(\nabla_{\vec{r}_i} A_{ijk} + \nabla_{\vec{r}_i} A_{ijl}) = \frac{1}{4}(\vec{e}_{jk}^\perp + \vec{e}_{lj}^\perp) \quad (42a)$$

$$\int \vec{K}_{ij} = \frac{1}{2}\varphi_{ij}\nabla_{\vec{r}_i} l_{ij} \quad (42b)$$

$$\int \vec{S}_{ij,1} = \frac{1}{2}l_{ij}\nabla_{\vec{r}_i}\varphi_{ij} = \frac{1}{2}(\cot\angle_{ijk}\vec{n}_{ijk} + \cot\angle_{ijl}\vec{n}_{ilj}) \quad (42c)$$

$$\int \vec{S}_{ij,2} = \frac{1}{2}(l_{jk}\nabla_{\vec{r}_i}\varphi_{jk} + l_{jl}\nabla_{\vec{r}_i}\varphi_{jl} + l_{ji}\nabla_{\vec{r}_i}\varphi_{ji}) = -\frac{1}{2}(\cot\angle_{jki}\vec{n}_{ijk} + \cot\angle_{ilj}\vec{n}_{ilj}), \quad (42d)$$

825 where the mean curvature vector, $\int \vec{H}$, results from area gradient; Gaussian curvature vector, $\int \vec{K}$, and the
 826 Schläfli vector, $\int \vec{S}$, consists of the two components of the variation of total mean curvature, $\frac{1}{2}\sum_{e_{ij}} l_{ij}\varphi_{ij}$. The
 827 asymmetry of vector quantities in Eq. (42) under index permutation (Eq. (40)) arises from the vertex we take
 828 the shape derivative with respect to (i.e., v_i , or v_j); because of the asymmetry, we can associate each Schläfli
 829 vector with a unique halfedge. Similar to the translation from edge values to vertex value (Eq. (9)), we can
 830 also translate the halfedge value to vertex value by summing all halfedge values over the fan neighborhood,

$$\int (\cdot)_i = \sum_{e_{ij} \in N(v_i)} \int (\cdot)_{ij}. \quad (43)$$

Note that unlike translating edge values, there is no prefactor 1/2 for translating halfedge values because each halfedge is uniquely associated with one vertex. The translated curvature vectors on a vertex can be compared against vertexwise smooth analytical solutions as benchmarked in Section 2.5.4. Now we have all of the elements needed to derive the derivatives of the discrete Willmore bending energy. Because the discrete energy is locally supported by the vertex, v_i , and its 1-ring neighbors, $v_j \in N(v_i)$, we can separate them into the “diagonal” term, and “off-diagonal” term,

$$\begin{aligned} \int \vec{f}_i^b &= -\nabla_{\vec{r}_i} E_b = -\nabla_{\vec{r}_i} \left(\sum_i \kappa_i (H_i(\vec{r}) - \bar{H}_i)^2 A_i(\vec{r}) \right) \\ &= \underbrace{-\nabla_{\vec{r}_i} [\kappa_i (H_i - \bar{H}_i)^2 A_i]}_{\text{diagonal}} - \underbrace{\sum_{v_j \in N(v_i)} \nabla_{\vec{r}_i} [\kappa_j (H_j - \bar{H}_j)^2 A_j]}_{\text{off-diagonal}}. \end{aligned} \quad (44)$$

Using the derivatives of geometric primitives in Eq. (41), we can assemble the derivatives of local pointwise mean curvature for both the “diagonal” term,

$$\begin{aligned} \nabla_{\vec{r}_i} H_i &= \frac{1}{4} \sum_{e_{ij} \in N(v_i)} \nabla_{\vec{r}_i} \frac{l_{ij}\varphi_{ij}}{A_i} \\ &= \frac{1}{4A_i} \sum_{e_{ij} \in N(v_i)} \left(\varphi_{ij}\nabla_{\vec{r}_i} l_{ij} + l_{ij}\nabla_{\vec{r}_i}\varphi_{ij} \right) - \frac{H_i}{A_i} \nabla_{\vec{r}_i} A_i \\ &= \frac{1}{A_i} \sum_{e_{ij} \in N(v_i)} \frac{1}{2} \left(\int \vec{K}_{ij} + \int \vec{S}_{ij,1} \right) - \frac{2}{3} H_i \int \vec{H}_{ij}, \end{aligned} \quad (45)$$

and for the “off-diagonal” term,

$$\begin{aligned} \nabla_{\vec{r}_i} H_j &= \frac{1}{4} \sum_{e_{jk} \in N(v_j)} \nabla_{\vec{r}_i} \frac{l_{jk}\varphi_{jk}}{A_j} \\ &= \frac{1}{4A_j} \left(l_{jk}\nabla_{\vec{r}_i}\varphi_{jk} + l_{jl}\nabla_{\vec{r}_i}\varphi_{jl} + \varphi_{ji}\nabla_{\vec{r}_i} l_{ji} + l_{ji}\nabla_{\vec{r}_i}\varphi_{ji} \right) - \frac{H_j}{A_j} \nabla_{\vec{r}_i} A_j \\ &= \frac{1}{2A_j} \left(\int \vec{K}_{ij} + \int \vec{S}_{ij,2} \right) - \frac{4}{3} H_j \int \vec{H}_{ij}. \end{aligned} \quad (46)$$

When written in the halfedge form, factoring out the fundamental curvature vectors introduced in Eq. (42), we obtain the discrete bending force as

$$\begin{aligned} \int f_i^b = & \sum_{e_{ij} \in N(v_i)} - [\kappa_i(H_i - \bar{H}_i) + \kappa_j(H_j - \bar{H}_j)] \int \vec{K}_{ij} \\ & + \left[\frac{1}{3} \kappa_i(H_i - \bar{H}_i)(H_i + \bar{H}_i) + \frac{2}{3} \kappa_j(H_j - \bar{H}_j)(H_j + \bar{H}_j) \right] \int 2\vec{H}_{ij} \\ & - \left[\kappa_i(H_i - \bar{H}_i) \int \vec{S}_{ij,1} + \kappa_j(H_j - \bar{H}_j) \int \vec{S}_{ij,2} \right]. \end{aligned} \quad (47)$$

831 C.3 Deriving the line tension and diffusion as the shape and chemical derivatives of the 832 Dirichlet energy

Since the discrete Dirichlet energy is constructed on the triangular face and therefore does not involve any neighborhood, we simplify the notation by adopting the convention illustrated in Fig. 1C. The gradient of protein density is given by the slope of the fitted plane over the vertexwise protein density, which is piecewise constant for each face,

$$\nabla_{\vec{\theta}} \phi_i = \frac{1}{2A_{ijk}} \sum_{\vec{e}_k \in N(f_{ijk})} \phi_k \vec{e}_k^\perp, \quad (48)$$

833 where we adopt the counterclockwise convention (e.g. $\vec{e}_k = \vec{e}_{ji}$) and $(\cdot)^\perp$ represents a 90° counterclockwise
834 rotation in plane of the face, f_{ijk} .

835 C.3.1 Line tension from the shape derivative of the Dirichlet energy

Substituting the definition of the discrete gradient into the Dirichlet energy (Eq. (28)), we expand the energy in terms of mesh primitives, whose geometric derivatives are given in Eq. (41). Additional formulae are needed to compute the geometric derivatives of the outer angles of the triangle (Fig. 1C)

$$\nabla_{\vec{r}_i} \angle_k = \frac{\vec{n} \times \vec{e}_j}{\|\vec{e}_j\|^2} \quad (49a)$$

$$\nabla_{\vec{r}_i} \angle_j = \frac{\vec{n} \times \vec{e}_k}{\|\vec{e}_k\|^2} \quad (49b)$$

$$\nabla_{\vec{r}_i} \angle_i = -(\nabla_{\vec{r}_i} \angle_k + \nabla_{\vec{r}_i} \angle_j), \quad (49c)$$

which arise from the calculation of the L_2 norm of the gradients as the result of vector inner product. When combined, the geometric derivatives for the quadratic gradient term is

$$\begin{aligned} \nabla_{\vec{r}_i} \left\langle \sum \phi_k \vec{e}_k^\perp, \sum \phi_k \vec{e}_k^\perp \right\rangle = & \\ & + \phi_k \phi_k \vec{e}_k - 2\phi_j \phi_j \vec{e}_j \\ & + 2\phi_j \phi_i \|\vec{e}_i\| \left(-\hat{e}_j \cos \angle_k + \|\vec{e}_j\| \nabla_{\vec{r}_i} (\cos \angle_k) \right) \\ & + 2\phi_i \phi_k \|\vec{e}_i\| \left(\hat{e}_k \cos \angle_j + \|\vec{e}_k\| \nabla_{\vec{r}_i} (\cos \angle_j) \right) \\ & + 2\phi_j \phi_k \left(-\hat{e}_j \|\vec{e}_k\| \cos \angle_i + \|\vec{e}_j\| \hat{e}_k \cos \angle_i + \|\vec{e}_j\| \|\vec{e}_k\| \nabla_{\vec{r}_i} (\cos \angle_i) \right) \end{aligned} \quad (50)$$

836 Then we can get the final shape derivative by combining the area gradient, or the mean curvature vector
837 (Eq. (42)).

838 C.3.2 Surface diffusion from the chemical derivative of the Dirichlet energy

839 In the case where we are evolving the protein distribution, we need the chemical derivative of the Dirichlet
 840 energy. Before we look into the discrete case, we can first tackle the problem in the smooth setting, which
 841 is a classic textbook example. Using the Green's first identity, or integration by parts on a 2-manifold,

$$\int_{\mathcal{M}} (\psi \Delta_s \varphi + \nabla_{\vec{\theta}} \psi \cdot \nabla_{\vec{\theta}} \varphi) dA = \oint_{\partial \mathcal{M}} \psi \nabla_{\vec{\theta}} \varphi \cdot \vec{n} dS, \quad (51)$$

842 and ignoring the boundary term at the right hand side, we arrive at an alternative expression for the Dirichlet
 843 energy,

$$E_d = \frac{1}{2} \int_{\mathcal{M}} \eta \|\nabla_{\vec{\theta}} \phi\|^2 dA = -\frac{1}{2} \int_{\mathcal{M}} \eta \phi \Delta_s \phi dA. \quad (52)$$

844 The same procedure can be followed in the discrete case. The discrete Dirichlet energy (Eq. (28)) can be
 845 written in matrix form,

$$E_d = \frac{1}{2} \eta \phi^\top \tilde{\mathbf{G}}^\top \tilde{\mathbf{T}} \tilde{\mathbf{G}} \phi \quad (53)$$

846 where $\tilde{\mathbf{G}}$ is the gradient tensor which maps scalar value on vertices to vector values on faces, and $\tilde{\mathbf{T}} =$
 847 $\text{diag}(\mathbf{A}^{\text{face}})$ is the $|f| \times |f|$ diagonal matrix with entries corresponding to the area of each mesh triangle face.
 848 Through integration by parts on a discrete geometry, the discrete Dirichlet energy can be equivalently ex-
 849 pressed as

$$E_d = \frac{1}{2} \eta \phi^\top \tilde{\mathbf{L}} \phi, \quad (54)$$

850 which is a quadratic form with respect to the cotangent Laplacian matrix, $\tilde{\mathbf{L}}$ (99, 100). The chemical derivative
 851 of the Dirichlet energy, or the diffusion potential, is

$$\mu^d = -\nabla_\phi E_d = -\eta \int \Delta_s \phi = -\eta \tilde{\mathbf{L}} \phi. \quad (55)$$

852 In other words, the chemical gradient flow of the Dirichlet energy is the diffusion equation. Note that $\tilde{\mathbf{L}} =$
 853 $\tilde{\mathbf{G}}^\top \tilde{\mathbf{T}} \tilde{\mathbf{G}}$, $\tilde{\mathbf{G}}^\top$ is referred to as the discrete divergence operator that maps face vectors to scalars on ver-
 854 tices (135).

855 D Discrete-smooth comparison on spheroid

The smooth-discrete comparison is done on the spheroid with the parametrization,

$$(x, y, z) = (a \cos \beta \cos \theta, a \cos \beta \sin \theta, c \sin \beta), \quad (56)$$

856 where $a = 1$, $b = 0.5$, β is the parametric latitude and θ is the azimuth coordinate. All geometric measurements
 857 of the smooth geometry used for benchmarking were obtained using the symbolic algebra software *Sympy*. The
 858 corresponding discrete measurements are computed using Mem3DG, whose input spheroid mesh is mapped
 859 from a subdivided icosphere. The subsequent error norms for local measurements are computed based on
 860 definitions used in Section 2.4.

861 E Mesh regularization and mesh mutation

862 E.1 Mesh mutation

863 Mesh mutation and refinement in combination with vertex shifting are the default methods to ensure that
 864 the mesh remains well-conditioned and well-resolved during simulation. Mesh mutations include edge flip-
 865 ping, collapsing, and splitting, changes the connectivity of the mesh. Vertex shifting moves the vertex to the

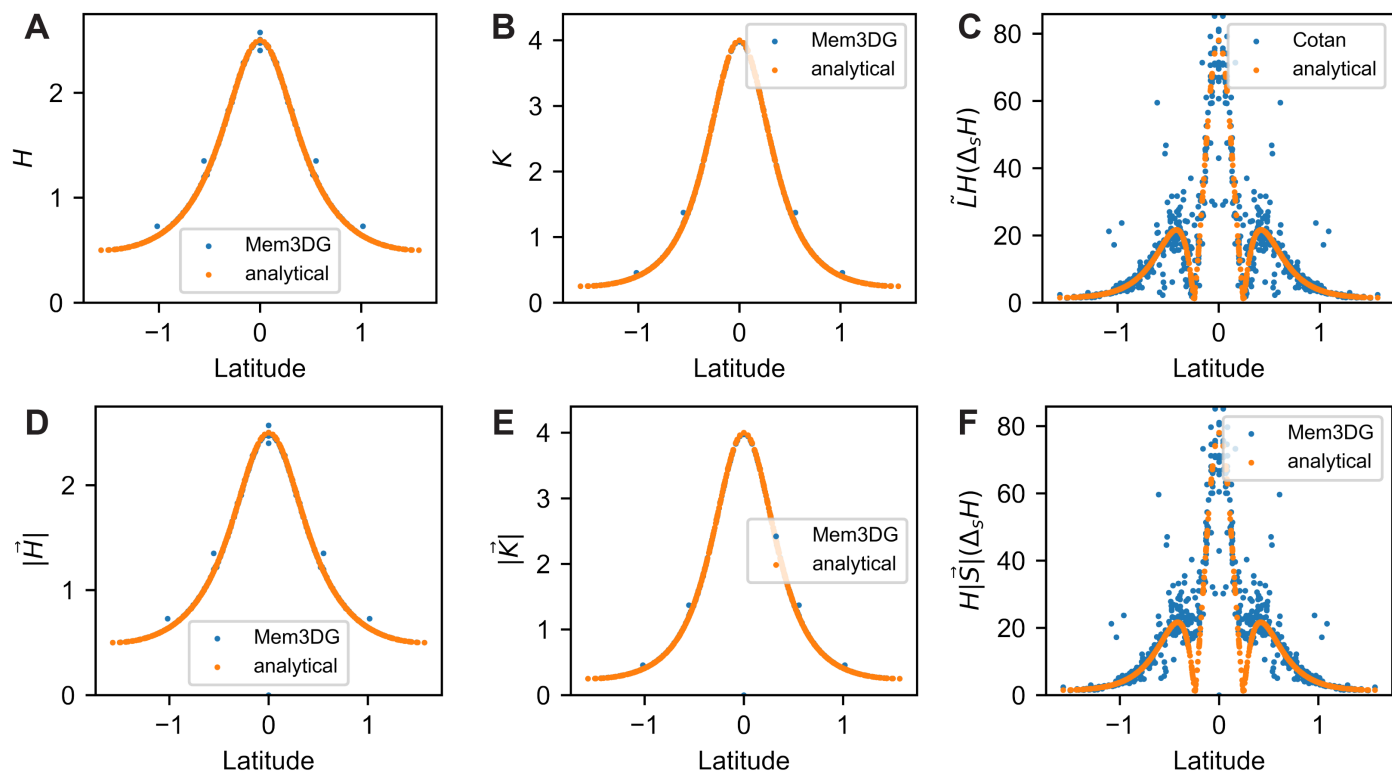


Figure E.1: Pointwise magnitude comparison of continuous and discrete measurements: A) scalar mean curvature, B) scalar Gaussian curvature, C) (scalar) bi-Laplacian term ∇H based on cotan formula, D) vector mean curvature, E) vector Gaussian curvature, and F) (vector) bi-Laplacian term based on Schläfli vector. Note that the result of the cotangent Laplacian approach in C) produces a scalar result while our approach using the Schläfli vector in F) is a vector result, thus their direct comparison is not meaningful.

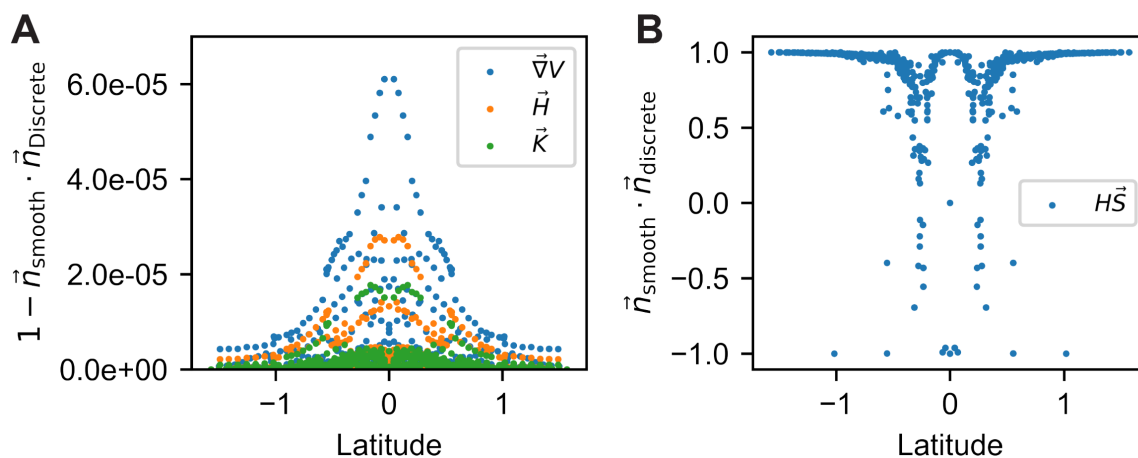


Figure E.2: Pointwise directional comparison of continuous and discrete measurements: discrete vertex normal based on A) volume gradient, $\nabla_{\vec{r}} V$, mean curvature vector, \vec{H} , and Gaussian curvature vector, \vec{K} , and B) Schläfli vector, $H\vec{S}$

866 barycenter of the fan neighborhood without changing the mesh topology (Fig. 1A). Mem3DG has a suite of possible
867 criteria to initiate mesh mutation. Here we list the most important ones: 1) flip the edge of non-Delaunay
868 diamond neighborhood (Fig. 1B), 2) collapse the shortest edge in a skinny triangle face, 3) split the edge with
869 high (geodesic) curvature. For additional details please refer to the software documentation.

870 For practical use, although mesh mutation introduces additional complexity in data writeout and computational
871 costs associated with varying (usually growing) mesh size, it nevertheless provides a robust algorithm
872 to ensure good mesh quality needed for valid discrete-smooth comparisons (Section 2.5.4) in static frames.
873 For dynamical simulation, mesh mutations introduce an arbitrary interpolation of state variables, such as the
874 position, velocity and protein density. Rigorous study on how to interpolate these quantities to ensure the
875 conservation of energy, momentum, and mass, remains to be done. Similarly, the interpolation used in this
876 study introduce discontinuities of curvature and can create jumps in forces; This is particularly severe for terms
877 with higher order derivatives such as the biharmonic term in bending force (Eq. (22)).

878 E.2 Mesh regularization

Mesh regularization can be used when mesh mutations are not desired. The regularization force consists of
three weakly enforced constraining forces, including the edge (length), \vec{f}^e , face (area), \vec{f}^f , and conformality
(angle), \vec{f}^c , regularization forces,

$$\vec{f}_i^e = -K_e \sum_{e_{ij} \in N(v_i)} \frac{(l_{ij} - \bar{l}_{ij})}{\bar{l}_{ij}} \nabla_{\vec{r}_i} l_{ij}, \quad (57a)$$

$$\vec{f}_i^f = -K_f \sum_{f_{ijk} \in N(v_i)} \frac{(A_{ijk} - \bar{A}_{ijk})}{\bar{A}_{ijk}} \nabla_{\vec{r}_i} A_{ijk}, \quad (57b)$$

$$\vec{f}_i^c = -K_c \sum_{e_{ij} \in N(v_i)} \frac{(\lambda_{ij} - \bar{\lambda}_{ij})}{\bar{\lambda}_{ij}} \nabla_{\vec{r}_i} \lambda_{ij}, \quad (57c)$$

879 which are in the order of strongest to weakest. The length-cross-ratio, $\lambda_{ij} = l_{il}l_{jk}/l_{ki}l_{jl}$ is a measure of
880 discrete conformality on triangulated mesh, where the indices is illustrated in Fig. 1A-B (136). Regularization
881 forces require the input of a reference value for geometric measures, \bar{l} , \bar{A} , and $\bar{\lambda}$, which can be derived from
882 a well-conditioned reference mesh (usually the initial input mesh for the simulation). The intensity of each
883 regularization force is controlled with parameters K_e , K_f , and K_c .

884 For practical use, regularization constraints should be minimally imposed because of their impact on system
885 dynamics. In the worst case regularization constraints can prevent the optimizer from reaching an energy
886 minima. Thus a good practice is to start a simulation in with no, conformality, face area, and finally edge length
887 regularization, and subsequently raise the intensity/type of constraints based on the mesh quality desired. We
888 do not recommend imposing constraints stronger than the face areal constraints, \vec{f}^f .

889 References

- 890 1. J. T. Groves, J. Kuriyan, *Nature structural & molecular biology* **17**, 659–665, ISSN: 1545-9993, DOI
891 [10/d37mbf](https://doi.org/10.1038/nstr.2010.10) (June 2010).
- 892 2. X. Cheng, J. C. Smith, *Chemical Reviews* **119**, 5849–5880, ISSN: 0009-2665, DOI [10/gfvk9g](https://doi.org/10.1021/acs.crev.9b00999) (May
893 2019).
- 894 3. M. Anitei, B. Hoflack, *Nature Cell Biology* **14**, 11–19, ISSN: 1476-4679, DOI [10/fox37b7](https://doi.org/10.1038/nrn2377) (Jan. 2012).
- 895 4. J. S. Bonifacino, B. S. Glick, *Cell* **116**, 153–166, ISSN: 0092-8674, 1097-4172, DOI [10/b7x4x3](https://doi.org/10.1016/S0092-8674(04)00100-0) (Jan.
896 2004).
- 897 5. J. M. Herrmann, A. Spang, in *Membrane Trafficking: Second Edition*, ed. by B. L. Tang (Springer, New
898 York, NY, 2015), pp. 1–12, ISBN: 978-1-4939-2309-0, DOI [10.1007/978-1-4939-2309-0_1](https://doi.org/10.1007/978-1-4939-2309-0_1).

- 899 6. H. T. McMahon, E. Boucrot, *Nature Reviews Molecular Cell Biology* **12**, 517–533, ISSN: 1471-0080,
900 DOI [10/b49pxb](https://doi.org/10.1038/nrm09555) (Aug. 2011).
- 901 7. J. Zimmerberg, M. M. Kozlov, *Nature Reviews Molecular Cell Biology* **7**, 9–19, ISSN: 1471-0080, DOI
902 [10/dfh54v](https://doi.org/10.1038/nrm09555) (Jan. 2006).
- 903 8. K. Farsad, P. D. Camilli, *Current Opinion in Cell Biology* **15**, 372–381, ISSN: 0955-0674, DOI [10/ctw22q](https://doi.org/10.1016/j.cob.2003.08.001)
904 (Aug. 2003).
- 905 9. O. Avinoam, M. Schorb, C. J. Beese, J. A. G. Briggs, M. Kaksonen, *Science* **348**, 1369–1372, ISSN:
906 0036-8075, 1095-9203, DOI [10.1126/science.aaa9555](https://doi.org/10.1126/science.aaa9555) (June 2015).
- 907 10. M. Terasaki *et al.*, *Cell* **154**, 285–296, ISSN: 00928674, DOI [10.1016/j.cell.2013.06.031](https://doi.org/10.1016/j.cell.2013.06.031) (July
908 2013).
- 909 11. Y. Shibata *et al.*, *Cell* **143**, 774–788, ISSN: 00928674, DOI [10.1016/j.cell.2010.11.007](https://doi.org/10.1016/j.cell.2010.11.007) (Nov.
910 2010).
- 911 12. H. T. McMahon, J. L. Gallop, *Nature* **438**, 590–596, ISSN: 1476-4687, DOI [10.1038/nature04396](https://doi.org/10.1038/nature04396)
912 (Dec. 2005).
- 913 13. H. T. McMahon, E. Boucrot, *Journal of Cell Science* **128**, 1065–1070, ISSN: 0021-9533, DOI [10/f64xp3](https://doi.org/10.1042/jcs.2014123)
914 (Mar. 2015).
- 915 14. M. M. Kozlov *et al.*, *Current Opinion in Cell Biology, Cell Organelles* **29**, 53–60, ISSN: 0955-0674, DOI
916 [10/f6f2f2](https://doi.org/10.1016/j.cob.2014.08.001) (Aug. 2014).
- 917 15. C. S. Scheve, P. A. Gonzales, N. Momin, J. C. Stachowiak, *Journal of the American Chemical Society*
918 **135**, 1185–1188, ISSN: 0002-7863, DOI [10.1021/ja3099867](https://doi.org/10.1021/ja3099867) (Jan. 2013).
- 919 16. J. C. Stachowiak, C. C. Hayden, D. Y. Sasaki, *Proceedings of the National Academy of Sciences* **107**,
920 7781–7786, ISSN: 0027-8424, 1091-6490, DOI [10.1073/pnas.0913306107](https://doi.org/10.1073/pnas.0913306107) (Apr. 2010).
- 921 17. J. C. Stachowiak *et al.*, *Nature Cell Biology* **14**, 944–949, ISSN: 1476-4679, DOI [10.1038/ncb2561](https://doi.org/10.1038/ncb2561)
922 (Sept. 2012).
- 923 18. J. C. Stachowiak, F. M. Brodsky, E. A. Miller, *Nature Cell Biology* **15**, 1019–1027, ISSN: 1476-4679,
924 DOI [10.1038/ncb2832](https://doi.org/10.1038/ncb2832) (Sept. 2013).
- 925 19. F. Yuan *et al.*, *Proceedings of the National Academy of Sciences* **118**, ISSN: 0027-8424, 1091-6490,
926 DOI [10.1073/pnas.2017435118](https://doi.org/10.1073/pnas.2017435118) (Mar. 2021).
- 927 20. M. Chabanon, J. C. Stachowiak, P. Rangamani, *Wiley Interdisciplinary Reviews: Systems Biology and*
928 *Medicine* **9**, e1386, ISSN: 19395094, DOI [10.1002/wsbm.1386](https://doi.org/10.1002/wsbm.1386) (Sept. 2017).
- 929 21. G. Knott, H. Marchman, D. Wall, B. Lich, *Journal of Neuroscience* **28**, 2959–2964, ISSN: 0270-6474,
930 1529-2401, DOI [10.1523/JNEUROSCI.3189-07.2008](https://doi.org/10.1523/JNEUROSCI.3189-07.2008) (Mar. 2008).
- 931 22. C. J. Peddie, L. M. Collinson, *Micron* **61**, 9–19, ISSN: 0968-4328, DOI [10.1016/J.MICRON.2014.01.009](https://doi.org/10.1016/j.micron.2014.01.009)
932 (June 2014).
- 933 23. B. Titze, C. Genoud, *Biology of the Cell* **108**, 307–323, ISSN: 02484900, DOI [10.1111/boc.201600024](https://doi.org/10.1111/boc.201600024)
934 (Nov. 2016).
- 935 24. G. Knott, C. Genoud, *Journal of Cell Science* **126**, 4545–4552, ISSN: 0021-9533, 1477-9137, DOI
936 [10.1242/jcs.124123](https://doi.org/10.1242/jcs.124123) (Oct. 2013).
- 937 25. K. D. Micheva, S. J. Smith, *Neuron* **55**, 25–36, ISSN: 0896-6273, DOI [10.1016/j.neuron.2007.06.014](https://doi.org/10.1016/j.neuron.2007.06.014)
938 (July 2007).
- 939 26. E. Villa, M. Schaffer, J. M. Plitzko, W. Baumeister, *Current Opinion in Structural Biology* **23**, 771–777,
940 ISSN: 0959440X, DOI [10.1016/j.sbi.2013.08.006](https://doi.org/10.1016/j.sbi.2013.08.006) (Oct. 2013).
- 941 27. J. Nixon-Abell *et al.*, *Science* (80-.), ISSN: 10959203, DOI [10.1126/science.aaf3928](https://doi.org/10.1126/science.aaf3928) (2016).
- 942 28. D. P. Hoffman *et al.*, *Science* **367**, ISSN: 0036-8075, 1095-9203, DOI [10.1126/science.aaz5357](https://doi.org/10.1126/science.aaz5357) (Jan.
943 2020).
- 944 29. C. S. Xu *et al.*, *Elife* **6**, ISSN: 2050-084X, DOI [10.7554/eLife.25916](https://doi.org/10.7554/eLife.25916) (May 2017).
- 945 30. T. G. Frey, C. A. Mannella, *Trends in Biochemical Sciences* **25**, 319–324, ISSN: 0968-0004, DOI [10/
946 dzjjnc](https://doi.org/10.1016/j.tics.2000.07.001) (July 2000).
- 947 31. Y. Wu *et al.*, *Proceedings of the National Academy of Sciences* **114**, E4859–E4867, ISSN: 0027-8424,
948 1091-6490, DOI [10.1073/pnas.1701078114](https://doi.org/10.1073/pnas.1701078114) (June 2017).

- 949 32. C. T. Lee *et al.*, *PLoS computational biology* **16**, e1007756 (2020).
- 950 33. R. Mendelsohn *et al.*, *Journal of Comparative Neurology*, cne.25254, ISSN: 0021-9967, 1096-9861,
951 DOI [10/gm72r9](https://doi.org/10/gm72r9) (Oct. 2021).
- 952 34. M. Salfer, J. F. Collado, W. Baumeister, R. Fernández-Busnadiego, A. Martínez-Sánchez, *PLOS Com-*
953 *putational Biology* **16**, e1007962, ISSN: 1553-7358, DOI [10/gmnx32](https://doi.org/10/gmnx32) (Aug. 2020).
- 954 35. H. Tamada, J. Blanc, N. Korogod, C. C. Petersen, G. W. Knott, *eLife* **9**, e56384, ISSN: 2050-084X, DOI
955 [10/gmqhr4](https://doi.org/10/gmqhr4) (Dec. 2020).
- 956 36. K. M. Davies *et al.*, *Proceedings of the National Academy of Sciences* **108**, 14121–14126, ISSN: 0027-
957 8424, 1091-6490, DOI [10.1073/pnas.1103621108](https://doi.org/10.1073/pnas.1103621108) (Aug. 2011).
- 958 37. K. M. Davies, C. Anselmi, I. Wittig, J. D. Faraldo-Gómez, W. Kühlbrandt, *Proceedings of the Na-*
959 *tional Academy of Sciences* **109**, 13602–13607, ISSN: 0027-8424, 1091-6490, DOI [10.1073/pnas.](https://doi.org/10.1073/pnas.1204593109)
960 [1204593109](https://doi.org/10.1073/pnas.1204593109) (Aug. 2012).
- 961 38. N. Ramakrishnan, P. B. Sunil Kumar, R. Radhakrishnan, *Physics Reports*, Mesoscale Computational
962 Studies of Membrane Bilayer Remodeling by Curvature-Inducing Proteins **543**, 1–60, ISSN: 0370-1573,
963 DOI [10.1016/j.physrep.2014.05.001](https://doi.org/10.1016/j.physrep.2014.05.001) (Oct. 2014).
- 964 39. W. Helfrich, *Zeitschrift für Naturforschung c* **28**, 693–703 (1973).
- 965 40. D. Steigmann, *Archive for Rational Mechanics and Analysis* **150**, 127–152 (1999).
- 966 41. F. Campelo, C. Arnarez, S. J. Marrink, M. M. Kozlov, *Advances in Colloid and Interface Science*, Special
967 Issue in Honour of Wolfgang Helfrich **208**, 25–33, ISSN: 0001-8686, DOI [10/f57v4s](https://doi.org/10/f57v4s) (June 2014).
- 968 42. H. Naito, M. Okuda, O.-Y. Zhong-can, *Physical Review Letters* **74**, 4345–4348, ISSN: 0031-9007, 1079-
969 7114, DOI [10.1103/PhysRevLett.74.4345](https://doi.org/10.1103/PhysRevLett.74.4345) (May 1995).
- 970 43. M. Deserno, *Chemistry and Physics of Lipids* **185**, 11–45, ISSN: 00093084, DOI [10.1016/j.chemphyslip.](https://doi.org/10.1016/j.chemphyslip.2014.05.001)
971 [2014.05.001](https://doi.org/10.1016/j.chemphyslip.2014.05.001) (Jan. 2015).
- 972 44. D. Argudo, N. P. Bethel, F. V. Marcoline, M. Grabe, *Biochimica et Biophysica Acta (BBA) - Biomem-*
973 *branes*, New Approaches for Bridging Computation and Experiment on Membrane Proteins **1858**,
974 1619–1634, ISSN: 0005-2736, DOI [10.1016/j.bbamem.2016.02.003](https://doi.org/10.1016/j.bbamem.2016.02.003) (July 2016).
- 975 45. D. Argudo, N. P. Bethel, F. V. Marcoline, C. W. Wolgemuth, M. Grabe, *Biophysical Journal* **112**, 2159–
976 2172, ISSN: 1542-0086, DOI [10.1016/j.bpj.2017.03.040](https://doi.org/10.1016/j.bpj.2017.03.040) (May 2017).
- 977 46. M. Hamm, M. Kozlov, *The European Physical Journal E* **3**, 323–335, ISSN: 1292-8941, DOI [10/cp87nn](https://doi.org/10/cp87nn)
978 (Dec. 2000).
- 979 47. A. Agrawal, D. J. Steigmann, *Continuum Mechanics and Thermodynamics* **21**, 57–82, ISSN: 0935-
980 1175, 1432-0959, DOI [10.1007/s00161-009-0102-8](https://doi.org/10.1007/s00161-009-0102-8) (June 2009).
- 981 48. P. Rangamani *et al.*, *Biomechanics and Modeling in Mechanobiology* **13**, 697–711, ISSN: 1617-7959,
982 1617-7940, DOI [10.1007/s10237-013-0528-6](https://doi.org/10.1007/s10237-013-0528-6) (Aug. 2014).
- 983 49. S. Liese *et al.*, *Proceedings of the National Academy of Sciences* **117**, 28614–28624, ISSN: 0027-8424,
984 1091-6490, DOI [10/gm3677](https://doi.org/10/gm3677) (Nov. 2020).
- 985 50. S. Liese, A. Carlson, *Biophysical Journal* **120**, 2482–2489, ISSN: 00063495, DOI [10/gm369j](https://doi.org/10/gm369j) (June
986 2021).
- 987 51. P. Bassereau *et al.*, *Journal of Physics D: Applied Physics* **51**, 343001, ISSN: 0022-3727, DOI [10.](https://doi.org/10.1088/1361-6463/aacb98)
988 [1088/1361-6463/aacb98](https://doi.org/10.1088/1361-6463/aacb98) (July 2018).
- 989 52. T. Baumgart, B. R. Capraro, C. Zhu, S. L. Das, *Annual Review of Physical Chemistry* **62**, 483–506,
990 ISSN: 0066-426X, 1545-1593, DOI [10/bzw68c](https://doi.org/10/bzw68c) (May 2011).
- 991 53. C. T. Lee, M. Akamatsu, P. Rangamani, *Current Opinion in Cell Biology* **71**, 38–45, ISSN: 09550674,
992 DOI [10.1016/j.ceb.2021.01.011](https://doi.org/10.1016/j.ceb.2021.01.011) (Aug. 2021).
- 993 54. A. E. Carlsson, *Current Opinion in Cell Biology*, Cell Architecture **50**, 1–7, ISSN: 0955-0674, DOI [10/](https://doi.org/10/gdnqms)
994 [gdnqms](https://doi.org/10/gdnqms) (Feb. 2018).
- 995 55. J. Liu, M. Kaksonen, D. G. Drubin, G. Oster, *Proceedings of the National Academy of Sciences* **103**,
996 10277–10282 (2006).
- 997 56. J. Liu, Y. Sun, D. G. Drubin, G. F. Oster, *PLoS biology* **7**, e1000204 (2009).

- 998 57. J. E. Hassinger, G. Oster, D. G. Drubin, P. Rangamani, *Proceedings of the national academy of sci-*
999 *ences* **114**, E1118–E1127 (2017).
- 1000 58. H. Alimohamadi, R. Vasan, J. E. Hassinger, J. C. Stachowiak, P. Rangamani, *Molecular biology of the*
1001 *cell* **29**, 2024–2035 (2018).
- 1002 59. M. Saleem *et al.*, *Nature Communications* **6**, 6249, ISSN: 2041-1723, DOI [10.1038/ncomms7249](https://doi.org/10.1038/ncomms7249) (May
1003 2015).
- 1004 60. M. Tachikawa, A. Mochizuki, *Proceedings of the National Academy of Sciences* **114**, 5177–5182, ISSN:
1005 0027-8424, 1091-6490, DOI [10.1073/pnas.1619264114](https://doi.org/10.1073/pnas.1619264114) (May 2017).
- 1006 61. R. Natesan, R. Radhakrishnan, in *Advances in Planar Lipid Bilayers and Liposomes* (Elsevier, 2015),
1007 vol. 22, pp. 129–175, ISBN: 978-0-12-802878-0, DOI [10.1016/bs.adplan.2015.06.004](https://doi.org/10.1016/bs.adplan.2015.06.004).
- 1008 62. N. J. Agrawal, R. Radhakrishnan, *Physical Review E* **80**, 011925, ISSN: 1539-3755, 1550-2376, DOI
1009 [10/bw4hpw](https://doi.org/10/bw4hpw) (July 2009).
- 1010 63. N. J. Agrawal, J. Nukpezah, R. Radhakrishnan, *PLoS Computational Biology* **6**, ed. by C. V. Rao,
1011 e1000926, ISSN: 1553-7358, DOI [10/bjppbr](https://doi.org/10/bjppbr) (Sept. 2010).
- 1012 64. R. Ma, J. Berro, *Biophysical Journal* **120**, 1625–1640, ISSN: 0006-3495, DOI [10/gm39f2](https://doi.org/10/gm39f2) (May 2021).
- 1013 65. A. Guckenberger, S. Gekle, *Journal of Physics: Condensed Matter* **29**, 203001, ISSN: 0953-8984,
1014 1361-648X, DOI [10.1088/1361-648X/aa6313](https://doi.org/10.1088/1361-648X/aa6313) (May 2017).
- 1015 66. M. Akamatsu *et al.*, *Elife* **9**, e49840 (2020).
- 1016 67. T. Willmore, *Riemannian Geometry* (Oxford University Press, 1996), ([https://books.google.com/](https://books.google.com/books?id=L6qtDAEACAAJ)
1017 [books?id=L6qtDAEACAAJ](https://books.google.com/books?id=L6qtDAEACAAJ)).
- 1018 68. E. A. Evans, *Mechanics and thermodynamics of biomembranes* (CRC press, 2018).
- 1019 69. P. B. Canham, *Journal of theoretical biology* **26**, 61–81 (1970).
- 1020 70. J. T. Jenkins, *SIAM Journal on Applied Mathematics* **32**, 755–764 (1977).
- 1021 71. J. T. Jenkins, *Journal of mathematical biology* **4**, 149–169 (1977).
- 1022 72. U. Seifert, *Advances in physics* **46**, 13–137 (1997).
- 1023 73. Q. Du, C. Liu, X. Wang, *Journal of Computational Physics* **198**, 450–468, ISSN: 0021-9991, DOI [10.](https://doi.org/10.1016/j.jcp.2004.01.029)
1024 [1016/j.jcp.2004.01.029](https://doi.org/10.1016/j.jcp.2004.01.029) (Aug. 2004).
- 1025 74. Q. Du, X. Wang, *International Journal of Numerical Analysis and Modeling* (2006).
- 1026 75. D. Salac, M. Miksis, *Journal of Computational Physics* **230**, 8192–8215 (2011).
- 1027 76. F. Feng, W. S. Klug, *Journal of Computational Physics* **220**, 394–408, ISSN: 00219991, DOI [10.1016/](https://doi.org/10.1016/j.jcp.2006.05.023)
1028 [j.jcp.2006.05.023](https://doi.org/10.1016/j.jcp.2006.05.023) (Dec. 2006).
- 1029 77. L. Ma, W. S. Klug, *Journal of Computational Physics* **227**, 5816–5835 (2008).
- 1030 78. C. M. Elliott, B. Stinner, *Journal of Computational Physics* **229**, 6585–6612, ISSN: 00219991, DOI
1031 [10.1016/j.jcp.2010.05.014](https://doi.org/10.1016/j.jcp.2010.05.014) (Sept. 2010).
- 1032 79. R. Rangarajan, H. Gao, *Journal of Computational Physics* **297**, 266–294, ISSN: 00219991, DOI [10.](https://doi.org/10.1016/j.jcp.2015.05.001)
1033 [1016/j.jcp.2015.05.001](https://doi.org/10.1016/j.jcp.2015.05.001) (Sept. 2015).
- 1034 80. R. A. Sauer, T. X. Duong, K. K. Mandadapu, D. J. Steigmann, *Journal of Computational Physics* **330**,
1035 436–466, ISSN: 00219991, DOI [10.1016/j.jcp.2016.11.004](https://doi.org/10.1016/j.jcp.2016.11.004) (Feb. 2017).
- 1036 81. R. Vasan, S. Rudraraju, M. Akamatsu, K. Garikipati, P. Rangamani, *Soft Matter* **16**, 784–797, ISSN:
1037 1744-683X, 1744-6848, DOI [10.1039/C9SM01494B](https://doi.org/10.1039/C9SM01494B) (Jan. 2020).
- 1038 82. A. Torres-Sánchez, D. Millán, M. Arroyo, *Journal of Fluid Mechanics* **872**, 218–271, ISSN: 0022-1120,
1039 1469-7645, DOI [10.1017/jfm.2019.341](https://doi.org/10.1017/jfm.2019.341) (Aug. 2019).
- 1040 83. D. Auddya *et al.*, “Biomembranes Undergo Complex, Non-Axisymmetric Deformations Governed by
1041 Kirchhoff-Love Kinematics and Revealed by a Three Dimensional Computational Framework”, Preprint
1042 (Biophysics, Jan. 2021), DOI [10.1101/2021.01.28.428578](https://doi.org/10.1101/2021.01.28.428578).
- 1043 84. G. Gompper, D. Kroll, *Journal de Physique I* **6**, 1305–1320 (1996).
- 1044 85. F. Jülicher, *Journal de physique ii* **6**, 1797–1824 (1996).
- 1045 86. Y. Kantor, D. R. Nelson, *Physical Review A* **36**, 4020 (1987).

- 1046 87. X. Bian, S. Litvinov, P. Koumoutsakos, *Computer Methods in Applied Mechanics and Engineering* **359**,
1047 112758, ISSN: 00457825, DOI [10.1016/j.cma.2019.112758](https://doi.org/10.1016/j.cma.2019.112758) (Feb. 2020).
- 1048 88. K. A. Brakke, *Experimental Mathematics* **1**, 141–165, ISSN: 1058-6458, 1944-950X, DOI [10.1080/
1049 10586458.1992.10504253](https://doi.org/10.1080/10586458.1992.10504253) (Jan. 1992).
- 1050 89. Y. Jie, L. Quanhui, L. Jixing, O.-Y. Zhong-Can, *Physical Review E* **58**, 4730–4736, ISSN: 1063-651X,
1051 1095-3787, DOI [10.1103/PhysRevE.58.4730](https://doi.org/10.1103/PhysRevE.58.4730) (Oct. 1998).
- 1052 90. D. M. Kroll, G. Gompper, *Science* **255**, 968–971, ISSN: 0036-8075, 1095-9203, DOI [10.1126/science.
1053 1546294](https://doi.org/10.1126/science.1546294) (Feb. 1992).
- 1054 91. E. Atilgan, S. X. Sun, *The Journal of Chemical Physics* **126**, 095102, ISSN: 0021-9606, 1089-7690,
1055 DOI [10.1063/1.2483862](https://doi.org/10.1063/1.2483862) (Mar. 2007).
- 1056 92. A. H. Bahrami, G. Hummer, *ACS Nano* **11**, 9558–9565, ISSN: 1936-0851, 1936-086X, DOI [10.1021/
1057 acsnano.7b05542](https://doi.org/10.1021/acsnano.7b05542) (Sept. 2017).
- 1058 93. H. Noguchi, G. Gompper, *Proceedings of the National Academy of Sciences* **102**, 14159–14164, ISSN:
1059 0027-8424, 1091-6490, DOI [10.1073/pnas.0504243102](https://doi.org/10.1073/pnas.0504243102) (Oct. 2005).
- 1060 94. K. Tsai *et al.*, *Physical Biology* **17**, 065011, ISSN: 1478-3975, DOI [10.1088/1478-3975/abb208](https://doi.org/10.1088/1478-3975/abb208) (Oct.
1061 2020).
- 1062 95. A. Guckenberger, M. P. Schraml, P. G. Chen, M. Leonetti, S. Gekle, *Computer Physics Communications*
1063 **207**, 1–23, ISSN: 00104655, DOI [10.1016/j.cpc.2016.04.018](https://doi.org/10.1016/j.cpc.2016.04.018) (Oct. 2016).
- 1064 96. J. R. Shewchuk, *Proc. 11th Int. Meshing Roundtable* **94720**, 115–126 (2002).
- 1065 97. W. Pezeshkian, M. König, S. J. Marrink, J. H. Ipsen, *Frontiers in molecular biosciences* **6**, 59 (2019).
- 1066 98. M. Sadeghi, T. R. Weigl, F. Noé, *The Journal of Chemical Physics* **148**, 044901, ISSN: 0021-9606,
1067 1089-7690, DOI [10.1063/1.5009107](https://doi.org/10.1063/1.5009107) (Jan. 2018).
- 1068 99. A. Chern, *Discrete Differential Geometry*, Nov. 19, 2020.
- 1069 100. K. Crane, *DISCRETE DIFFERENTIAL GEOMETRY: AN APPLIED INTRODUCTION*, Apr. 13, 2020.
- 1070 101. E. A. Evans, *Biophysical Journal* **14**, 923–931, ISSN: 0006-3495, DOI [10/fftb7r](https://doi.org/10/fftb7r) (Dec. 1974).
- 1071 102. M. P. Do Carmo, *Differential geometry of curves and surfaces: revised and updated second edition*
1072 (Courier Dover Publications, 2016).
- 1073 103. J. M. Lee, *Introduction to Smooth Manifolds* (Springer New York, New York, NY, 2012), vol. 218, ISBN:
1074 978-1-4419-9981-8, DOI [10.1007/978-1-4419-9982-5](https://doi.org/10.1007/978-1-4419-9982-5).
- 1075 104. R. Phillips, J. Kondev, J. Theriot, *Physical Biology of the Cell* (Garland Science, Taylor & Francis Group,
1076 New York, Nov. 2008), ISBN: 978-0815341635, ([http://www.worldcat.org/search?qt=worldcat_
1077 org_all&q=0815341636](http://www.worldcat.org/search?qt=worldcat_org_all&q=0815341636)).
- 1078 105. M. Meyer, M. Desbrun, P. Schröder, A. H. Barr, in *Visualization and Mathematics III*, ed. by G. Farin
1079 *et al.* (Springer Berlin Heidelberg, Berlin, Heidelberg, 2003), pp. 35–57, ISBN: 978-3-642-05682-6, DOI
1080 [10.1007/978-3-662-05105-4_2](https://doi.org/10.1007/978-3-662-05105-4_2).
- 1081 106. M. Wardetzky, S. Mathur, F. Kälberer, E. Grinspun, presented at the ACM SIGGRAPH ASIA 2008
1082 Courses on - SIGGRAPH Asia '08, pp. 1–5, DOI [10.1145/1508044.1508063](https://doi.org/10.1145/1508044.1508063).
- 1083 107. M. Wardetzky, in *Discrete Differential Geometry*, ed. by A. I. Bobenko, J. M. Sullivan, P. Schröder,
1084 G. M. Ziegler (Birkhäuser Basel, Basel, 2008), vol. 38, pp. 275–286, ISBN: 978-3-7643-8620-7, DOI
1085 [10.1007/978-3-7643-8621-4_15](https://doi.org/10.1007/978-3-7643-8621-4_15).
- 1086 108. M. Deserno.
- 1087 109. N. Sharp, K. Crane, *et al.*, *geometry-central*, www.geometry-central.net, 2019.
- 1088 110. N. Sharp, K. Crane, *et al.*, *hapPLY*, <https://github.com/nmwsharp/happly>, 2018.
- 1089 111. R. Rew, G. Davis, *IEEE computer graphics and applications* **10**, 76–82 (1990).
- 1090 112. N. Sharp *et al.*, *Polyscope*, www.polyscope.run, 2019.
- 1091 113. W. Jakob, J. Rhineland, D. Moldovan, *pybind11 – Seamless operability between C++11 and Python*,
1092 <https://github.com/pybind/pybind11>, 2017.
- 1093 114. J. Nocedal, S. J. Wright, *Numerical Optimization* (Springer, New York, 2nd ed, 2006), ISBN: 978-0-387-
1094 30303-1.

- 1095 115. T. J. Hughes, *The finite element method: linear static and dynamic finite element analysis* (Courier
1096 Corporation, 2012).
- 1097 116. F. Jülicher, R. Lipowsky, *Physical Review E* **53**, 2670 (1996).
- 1098 117. H. Deuling, W. Helfrich, *Biophysical journal* **16**, 861 (1976).
- 1099 118. E. Evans, Y.-C. Fung, *Microvascular Research* **4**, 335–347, ISSN: 0026-2862, DOI [10.1016/0026-](https://doi.org/10.1016/0026-2862(72)90069-6)
1100 [2862\(72\)90069-6](https://doi.org/10.1016/0026-2862(72)90069-6) (1972).
- 1101 119. H. Alimohamadi, A. S. Smith, R. B. Nowak, V. M. Fowler, P. Rangamani, *bioRxiv*, 668582, DOI [10.](https://doi.org/10.1101/668582)
1102 [1101/668582](https://doi.org/10.1101/668582) (Nov. 2019).
- 1103 120. H.-H. Gerdes, R. N. Carvalho, *Current opinion in cell biology* **20**, 470–475 (2008).
- 1104 121. K. M. Pearce *et al.*, *Molecular Biology of the Cell* **31**, 683–694, ISSN: 1059-1524, DOI [10.1091/mbc.](https://doi.org/10.1091/mbc.E19-09-0536)
1105 [E19-09-0536](https://doi.org/10.1091/mbc.E19-09-0536) (Mar. 2020).
- 1106 122. H. Alimohamadi, B. Ovrzyn, P. Rangamani, *Scientific reports* **10**, 1–15 (2020).
- 1107 123. A. Datar *et al.*, *Biophysical Journal* **117**, 880–891, ISSN: 00063495, DOI [10.1016/j.bpj.2019.07.046](https://doi.org/10.1016/j.bpj.2019.07.046)
1108 (Sept. 2019).
- 1109 124. P. A. Pullarkat, P. Dommersnes, P. Fernández, J.-F. Joanny, A. Ott, *Physical Review Letters* **96**,
1110 048104, ISSN: 0031-9007, 1079-7114, DOI [10.1103/PhysRevLett.96.048104](https://doi.org/10.1103/PhysRevLett.96.048104) (Feb. 2006).
- 1111 125. J. Plateau, *Experimental and Theoretical Statics of Liquids Subject to Molecular Forces Only*, 1873.
- 1112 126. L. Rayleigh, *On the Instability of Jets*, 1878.
- 1113 127. O.-Y. Zhong-can, W. Helfrich, *Physical Review A*, 9.
- 1114 128. R. Bar-Ziv, E. Moses, *Physical review letters* **73**, 1392 (1994).
- 1115 129. J. Sanborn, K. Oglecka, R. S. Kraut, A. N. Parikh, *Faraday Discuss.* **161**, 167–176, ISSN: 1359-6640,
1116 1364-5498, DOI [10.1039/C2FD20116J](https://doi.org/10.1039/C2FD20116J) (2013).
- 1117 130. S. Watanabe *et al.*, *Nature* **504**, 242–247, ISSN: 1476-4687, DOI [10.1038/nature12809](https://doi.org/10.1038/nature12809) (Dec. 2013).
- 1118 131. T. Baumgart, S. T. Hess, W. W. Webb, *Nature* **425**, 821–824, ISSN: 0028-0836, 1476-4687, DOI [10.](https://doi.org/10.1038/nature02013)
1119 [1038/nature02013](https://doi.org/10.1038/nature02013) (Oct. 2003).
- 1120 132. K. Crane, C. Weischedel, M. Wardetzky, *Communications of the ACM* **60**, 90–99, ISSN: 00010782,
1121 DOI [10.1145/3131280](https://doi.org/10.1145/3131280) (Oct. 2017).
- 1122 133. D. Serwas *et al.*, “Actin Force Generation in Vesicle Formation: Mechanistic Insights from Cryo-Electron
1123 Tomography”, Preprint (Cell Biology, June 2021), DOI [10.1101/2021.06.28.450262](https://doi.org/10.1101/2021.06.28.450262).
- 1124 134. J. Steiner, in *Jacob Steiner’s Gesammelte Werke: Herausgegeben auf Veranlassung der königlich*
1125 *preussischen Akademie der Wissenschaften*, ed. by K. Weierstrass (Cambridge University Press, 2013),
1126 vol. 2, pp. 171–176, DOI [10.1017/CB09781139567947.016](https://doi.org/10.1017/CB09781139567947.016).
- 1127 135. A. Jacobson, D. Panozzo, *et al.*, *libigl: A simple C++ geometry processing library*, <https://libigl.github.io/>,
1128 2018.
- 1129 136. Y. Soliman *et al.*, *ACM Trans. Graph.* **40**, ISSN: 0730-0301, DOI [10.1145/3450626.3459759](https://doi.org/10.1145/3450626.3459759), ([https:](https://doi.org/10.1145/3450626.3459759)
1130 [//doi.org/10.1145/3450626.3459759](https://doi.org/10.1145/3450626.3459759)) (July 2021).